Atmos. Chem. Phys. Discuss., https://doi.org/10.5194/acp-2018-1312
Manuscript under review for journal Atmos. Chem. Phys.
Discussion started: 7 January 2019

Atmospheric Chemistry and Physics
Discussions

Tropical Pacific Climate Variability under Solar Geoengineering: Impacts on ENSO Extremes

Abdul Malik[1,2], Peer J. Nowack[1,3,4], Joanna D. Haigh[1,3], Long Cao[5], Luqman Atique[5], Yves Plancherel[1]

[1]Grantham Institute – Climate Change and the Environment, Imperial College London, London, United Kingdom
[2]Oeschger Centre for Climate Change Research, and Institute of Geography, University of Bern, Bern, Switzerland
[3]Department of Physics, Blackett Laboratory, Imperial College London, United Kingdom
[4]Data Science Institute, Imperial College London, United Kingdom
[5]School of Earth Sciences, Zhejiang University, Hangzhou, China

Correspondence to: Abdul Malik (a.malik@imperial.ac.uk)

Abstract

Many modelling studies suggest that the El Niño Southern Oscillation (ENSO), in interaction with the tropical Pacific background climate, will change under rising atmospheric greenhouse gas concentrations. Solar geoengineering (reducing the solar flux from outer space) has been proposed as a means to counteract anthropogenic greenhouse-induced changes in climate. Effectiveness of solar geoengineering is uncertain. Robust results are particularly difficult to obtain for ENSO because existing geoengineering simulations are too short (typically ~50 years) to detect statistically significant changes in the highly variable tropical Pacific background climate. We here present results from a 1000-year sunshade geoengineering simulation, G1, carried out with the coupled atmosphere-ocean general circulation model HadCM3L. In agreement with previous studies, reducing the shortwave solar flux more than compensates the warming in the tropical Pacific that develops in the 4×CO_2 scenario: we observe an overcooling of 0.3°C (5 %) and 0.23-mm day^{-1} (5 %) reduction in mean rainfall relative to preindustrial conditions in the G1 simulation. This is due to the different latitudinal distributions of the shortwave (solar) and longwave (CO_2) forcings.The location of the Intertropical Convergence Zone (ITCZ) located north of equator in the tropical Pacific, which moved 7.5° southwards under 4×CO_2, is also restored to its preindustrial location. However, other aspects of the tropical Pacific mean climate are not reset as effectively. Relative to preindustrial conditions, in G1 the zonal wind stress, zonal sea surface temperature (SST) gradient, and meridional SST gradient are reduced by 10 %, 11 %, and 9 %, respectively, and the Pacific Walker Circulation (PWC) is consistently weakened. The overall amplitude of ENSO strengthens by 5-8 %, but there is a 65 % reduction in the asymmetry between cold and warm events: cold events intensify more than warm events. Importantly, the frequency of extreme El Niño and La Niña events increases by 44 % and 32 %, respectively, while the total number of El Niño events increases by 12 %. Paradoxically, while the number of total and extreme events increase, the most extreme El Niño events also become weaker relative to preindustrial state while the La Niña events become stronger. That is, extreme El Niño events in G1 become less extreme than in preindustrial conditions, but extreme El Niño events become more frequent. In contrast,

extreme La Niña events become stronger in G1. This is in agreement with the general overcooling of the tropical Pacific in G1 relative to preindustrial conditions, which depict a shift towards generally more La Niña-like conditions.

1 Introduction

Since the industrial revolution the increasing concentrations of Greenhouse Gases (GHGs) are mainly responsible for higher global surface temperatures (Stocker 2013). Higher temperatures in turn, and more generally a rapidly changing climate, can have adverse effects on humans, plants, and animals through changes in various ecosystems, rising sea levels, melting glaciers, and could significantly impact the frequency and intensity of extreme weather events (Moore et al., 2015).

Various strategies, principally a reduction in emissions of GHGs and enhancing the carbon sinks (Pachauri et al. 2014), have been proposed to mitigate anthropogenic climate change. Another group of strategies involving the intentional modification of Earth's radiation balance on a global scale, known as geoengineering or climate engineering, have been proposed to overcome the negative consequences of human-induced GHGs (Crutzen 2006; Wigley 2006; Curry et al., 2014). For any serious consideration of such geoengineering strategies, it is essential to understand their potential benefits and perils. The principal route to study potential impacts of geoengineering on various components of Earth's climate system (e.g., atmosphere, ocean, cryosphere etc.) is employing state-of-the-art coupled atmosphere-ocean general circulation models (AOGCMs).

In this context, Kravitz et al. (2011) proposed the Geo-engineering Model Intercomparison Project (GeoMIP) which originally consisted of a set of four experiments (viz. G1, G2, G3, and G4). These experiments are designed to understand the effects of geoengineering on the regional and global climate by balancing the annual mean global radiative forcing at the top of the Earth's atmosphere, approximately offsetting global mean surface warming. These experiments are collectively called Solar Radiation Management (SRM) or solar geoengineering (Kravitz et al., 2013a). In the G1 experiment, atmospheric CO_2 is instantaneously quadrupled but the global GHGs-induced longwave radiative effects are offset by a simultaneous reduction in the shortwave Total Solar Irradiance, TSI, (Kravitz et al., 2011). In terms of radiative forcing, quadrupling of CO_2 is similar to year 2100 in the RCP8.5 emission scenario (Representative Concentration Pathway with a radiative forcing of 8.5 W m^{-2} by the year 2100; Schmidt et al., 2012). In this paper we focus on G1 experiment to investigate how effectively solar geoengineering could mitigate the effects of large changes in atmospheric CO_2 on tropical Pacific climate?

The El Niño Southern Oscillation (ENSO) is an important coupled ocean-atmosphere mode of interannual variability in the tropical Pacific (Park et al., 2009; Vecchi and Wittenberg 2010) which affects both regional and global climate (see Ropelewski and Halpert 1987; Bove et al, 1998; Malik et al., 2017). ENSO oscillates between a warm, El Niño, and a cold, La Niña, phase every 2-7-years (Santoso et al., 2017). As diagnosed from Sea Surface Temperature (SST) indices in state-of-the-art AOGCMs, there is no consensus about change

Atmos. Chem. Phys. Discuss., https://doi.org/10.5194/acp-2018-1312
Manuscript under review for journal Atmos. Chem. Phys.
Discussion started: 7 January 2019

in frequency of ENSO events in a warming climate (Vega-Westhoff and Sriver 2017; Yang et al., 2018). However, Cai et al. (2014 and 2015b) showed evidence of a doubling of El Niño and La Niña events in the Coupled Model Intercomparison Project (CMIP) phases 3 (A2 scenario) and 5 (RCP8.5) by investigating a performance-based subset of models using rainfall-based ENSO indices instead of SST-based indices. Similarly, Wang et al. (2017) also observed doubling of extreme El Niño events, relative to preindustrial level, in the RCP2.6 transient scenario a century after stabilization of global mean temperature. While models agree that the frequency will increase, the response of the amplitude of ENSO is less clear. Chen et al. (2017), analyzing 20 CMIP5 models (RCP8.5), found both strengthening (in 6 models) and weakening (in 8 models) of ENSO amplitude. In summary, changes in ENSO characteristics such as amplitude, and ENSO extremes are projected in a warming climate (e.g., Cai et al., 2014 and 2015b; Kim et al., 2014; Wang et al., 2018). In the present work we investigate the potential of solar geoengineering to mitigate changes in the amplitude and in the frequency of extreme ENSO events, essentially asking if decreasing the downwelling shortwave radiative flux can balance the GHGs-induced longwave effects on ENSO.

Increasing GHGs have distinct effects on the tropical Pacific mean climate. In CMIP3 and CMIP5 simulations, the equatorial tropical Pacific consistently shows an El Niño-like mean-response to increased GHG forcing (van Oldenborgh et al., 2005; Collins et al., 2010; Vecchi and Wittenberg et al., 2010; Huang and Ying et al., 2015; Luo et al., 2015). Models also show more warming on than off the equatorial tropical Pacific (Liu et al., 2005; Collins et al., 2010; Cai et al., 2015a). Consistent with these warming patterns, studies typically found a weakening of Pacific Walker Circulation (PWC), zonal SST gradient (ZSSTG), zonal wind stress, and a shoaling of the equatorial tropical Pacific thermocline (see van Oldenborgh et al., 2005; Latif et al., 2009; Park et al., 2009; Yeh et al., 2009; Collins et al., 2010; Kim et al., 2014; Cai et al., 2015a; Zhou et al., 2015; Vega-Westhoff and Sriver 2017; Wang et al., 2017). Changes in the mean state of the tropical Pacific can bring about variations in ENSO properties such as amplitude, frequency, and spatial pattern (Collins et al 2010; Vecchi and Wittenberg 2010; Cai et al., 2015a).

Since increasing GHG forcing affects circulation patterns related to tropical Pacific and the mean state of tropical Pacific Ocean, a detailed investigation is required to know if the region returns to preindustrial conditions in the solar geoengineering scenario. Guo et al. (2018) found no statistically significant change in the intensity of Walker Circulation relative to preindustrial conditions in the G1 experiment in GeoMIP models, and Gabriel and Robock (2015) similarly found no statistically significant change in frequency and amplitude of ENSO events under both global warming and geoengineering scenarios in the 6 GeoMIP models that captured ENSO variability best. However, this could be attributed to the short length (50 years) of the GeoMIP simulations used in the analyses, meaning that longer simulations are needed to detect any possible subtle changes in a statistically significant manner. Guo et al. (2018) concluded that 60 or more years of model simulations are required to detect changes in the PWC, while Vecchi et al. (2006) and Vecchi and Soden (2007) argue that 130 years are required to detect any robust change in the PWC (Gabriel and Robock 2015). According to Stevenson et al. (2010), 250 years are required to detect changes in ENSO variability with a statistical significance of 90 %. Long-term geoengineering simulations are clearly necessary to detect changes in extreme weather events and modes of internal climate variability.

We here examine the impacts of geoengineering on tropical Pacific mean climate and ENSO variability in 1000-year simulations of HadCM3L (Cox et al., 2000), the same model used by Cao et al. (2016) and Cai et. al. (2014). Cai et. al. (2014) had performed 33 perturbed physics experiments with HadCM3L and found that the frequency of El Niño events increases under global warming scenario, consistent with other 9 CMIP3 and 11 CMIP5 simulations. Using HadCM3L, we investigate the extent to which decreasing the downward shortwave radiative flux by solar geoengineering can mitigate or minimize the changes in frequency of extreme ENSO events and amplitude that are triggered by increasing greenhouse forcing. We acknowledge that some of our results are necessarily model-dependent, but by using a much longer simulations than used previously, our results provide statistical robustness for the given model system. Specifically, we ask (1) if solar geoengineering can mitigate the changes in mean tropical Pacific climate found in previous GHG warming studies, and even bring it back to the preindustrial conditions, (2) if ENSO frequency and amplitude are different under G1 conditions than under preindustrial simulations, and (3) if the G1 experiment reduces the doubling in frequency of extreme ENSO events, as observed by Cai et al. (2014 and 2015b) under increased GHG forcing, relative to the preindustrial state.

Section 2 describes the data and statistical methods used to detect changes in tropical Pacific and ENSO variability. Section 3 evaluates the response of a list of metrics used to understand how the mean state and ENSO variability are affected in the different experiments (preindustrial, 4xCO_2, G1). Finally Sect. 4 presents discussion and conclusion.

2 Data and methods

2.1 Climate model

HadCM3L has a horizontal resolution of 3.75^o × 2.5^o (~T42) with 19 (L19) atmospheric and 20 (L20) ocean levels. Land surface processes are simulated by the MOSES-2 module (Essery and Clark 2003; Cao et al., 2016). HadCM3L does not include an interactive atmospheric chemistry scheme and thus does not consider the potential effects of ozone changes on ENSO amplitudes and surface warming under 4xCO2 (e.g., Nowack et al., 2015; 2017, 2018) or G1 (e.g., Nowack et al., 2016). Instead we use a preindustrial background ozone climatology, prescribed on pressure levels.

HadCM3L is capable of reproducing present-day ENSO periodicity, teleconnection patterns, and amplitude (Collins et al., 2001). There is a non-linear relationship between tropical Pacific SST and rainfall (Ham 2017) which can be diagnosed by Niño3 region (5^{o}N-5^{o}S; 150^{o}W-90^{o}W) rainfall skewness. During extreme El Niño events, the northern part of tropical Pacific Intertropical Convergence Zone (ITCZ) moves equatorward, causing significant increases in rainfall (> 5 mm day^{-1}) over the eastern equatorial Pacific that biases (skews) the statistical distribution of rainfall in the Niño3 region. Thus, for studying extreme ENSO events the model should be capable of simulating Niño3 rainfall above 5 mm day^{-1} and Niño3 rainfall skewness of greater than 1 (see our Sect. 3.2.2, and Cai et al., 2014 and 2015b). With a Niño3 rainfall skewness of 2.06 for the preindustrial control, HadCM3L fulfills this criterion.

2.2 Simulations and observational data

To achieve a quasi-equilibrium preindustrial climate state, the model was spun up for 3000 years with constant CO_2 concentrations (280 ppm; parts per million) and TSI (1365 W m^{-2}). Then, three 1000-yr long experiments were carried out, starting from this preindustrial climate state. These experiments are: (1) the preindustrial control (piControl) experiment with constant values of CO_2 (280 ppm) and TSI (1365W m^{-2}), (2) a quadrupled CO_2 (4×CO_2) experiment in which CO_2 is suddenly increased to 1120 ppm, and (3) a sun-shade geoengineering (G1) experiment where the radiative effects of the instantaneously quadrupled CO_2 are offset by simultaneously reducing TSI (by 4 %). All experiments follow the GeoMIP protocol (see Kravitz et al., 2011); the only difference being that simulations were run for 1000 years (Cao et al., 2016).

Next to the simulations, we also use observational datasets: we employ the monthly SST dataset from HadISST (Rayner et al., 2003) and the rainfall data from the Global Precipitation Climatology Project (GPCP; Adler et al., 2003) over the period 1979-2017 to obtain observational constraints and to identify the rainfall threshold to be used for defining extreme El Niño events in climate model simulations.

2.3 Definitions and statistical tests

We analyze changes in the tropical Pacific (25° N-25° S; 90° E-60° W) mean climate. We present mean climatologies for SSTs, rainfall, ITCZ, vertical velocity averaged between 500 and 100 hPa (Omega 500-100), PWC, zonal wind stress, zonal and meridional SST ggradients (ZSSTG and MSSTG), and thermocline depth. The difference of mean climatology of all these variables simulated under 4×CO_2, and G1 is calculated relative to the piControl. The statistical significance of climatological mean values and their difference with piControl is tested using non-parametric Wilcoxon Signed rank and Wilcoxon rank sum tests (Hollander and Wolfe 1999; Gibbons and Chakraborti 2011), respectively. All analyses are performed on re-gridded (2° longitude × 2.5° latitude) HadCM3L output from model years 11 to 1000. The first 10 years are skipped to remove the initally large atmospheric transient effects stemming from instantaneously increasing CO_2 (see Kravitz et al., 2013b; Hong et al., 2017). Since ENSO events peak in boreal winter (December-January-February; DJF; Cai et al., 2014, Gabriel and Robock 2015; Santoso et al., 2017) the entire analysis is performed for DJF. Accordingly, we also analyze mean state changes in the tropical Pacific during boreal winter.

Both rainfall and SST-based ENSO indices are used in the present study. Niño3 (5° N-5° S; 150° W-90° W), Niño4 (5° N-5° S; 160° E-150° W), and Niño3.4 (5° N-5° S; 170° W-120° W) indices are defined by averaging SST over corresponding ENSO regions. Normalized ENSO anomalies (i.e. the ENSO indices) are calculated relative to piControl mean and standard deviation (s.d.) and are quadratically detrended before analysis. The Niño3 index is chosen for studying the characteristics of extreme El Niño events, since during an extreme El Niño event, following the highest SSTs, convective activity moves towards the eastern Pacific and the ITCZ moves over the Niño3 region resulting in anomalous rainfall (Cai et al., 2014). Similarly to Cai et al. 2014, events with Niño3 rainfall greater than 5 mm day^{-1} are considered extreme El Niño events, whereas events with Niño3 SST index greater than 0.5 s.d. and Niño3 rainfall less than 5 mm day^{-1} are defined as moderate. The Niño4 index is chosen for studying the characteristics of extreme La Niña events, since maximum cold temperatures occur in this region (Cai et al., 2015a, 2015b). La Niña extreme (Niño4 < -1.75 s.d.), moderate (-1 > Niño4 > -1.75), and weak (-0.5 > Niño4 > -1) events are defined following Cai et al. (2015b). These definitions classify the 1988 and 1998 La Niñas in observations as extreme events (see Cai et al., 2015b) and HadCM3L can reproduce such extreme anomalies (see Sect. 3.2.3), which allows us to study changes in their number and magnitude for our model system. Following Cai et al. (2014), the statistical significance of the change in frequency of ENSO events is tested using a bootstrap method with 10,000 realizations. The piControl time series is sampled 10,000 times, allowing for resampling. We then find the s.d. of events in 10,000 realizations. If the difference of events between piControl and G1 is larger than 2 s.d. the change in frequency is considered statistically significant. The same method is used for testing the statistical significance of change in amplitude, ZSSTG, meridional SST gradient (MSSTG), and ENSO amplitude asymmetry. All comparisons of 4×CO_2 and G1 are made relative to piControl.

3 Results

3.1 Changes in the tropical Pacific mean state

In this section, we analyse several important changes in the tropical Pacific mean state under 4xCO_2 and G1 relative to the preindustrial simulation. In particular, we look into meridional and zonal SST changes, corresponding surface wind responses and also coupled changes in the thermocline depth. We also show that this leads to significant differences in the precipitation climatology among the simulations. Finally, we find consistent differences in the Walker Circulation, as for example evident from changes in the vertical velocities in the tropical West Pacific upwelling region. All these differences are important not just as general climatic features but are additionally linked to changes in ENSO extremes discussed in detail in Sect. 3.2.

3.1.1 Sea surface temperature

The tropical Pacific SSTs are spatially asymmetric along the equator. The western equatorial Pacific (warm pool) is warmer on average than the eastern equatorial Pacific (cold tongue) (Vecchi and Wittenberg 2010). In HadCM3L, the piControl simulation depicts this SST asymmetry between the western and eastern equatorial Pacific well (Fig. 1a). Under 4×CO_2 this SST zonal asymmetry is significantly reduced (Fig. 1b), and the tropical Pacific resembles a persistent El Niño-like warming state (e.g., Meehl and Washington 1996; Boer et al., 2004) on top of a general background level of warming. The solar dimming in G1 offsets the warming observed under 4×CO_2 and brings the tropical Pacific mean SSTs close to the preindustrial state (Fig. 1c). The South Pacific Convergence Zone (SPCZ), where the highest

SSTs of the warm pool occur (Cai et al., 2015a; red line in Fig. 1a), moves towards the equator under 4xCO_2 (red line, Fig. 1b), but returns to approximately its preindustrial position in G1 (Fig. 1c).

The tropical Pacific is 3.90 ^{o}C warmer than piControl in 4×CO_2 but 0.30 ^{o}C colder in G1, with the difference being significant at the 99 % confidence level (hereafter "cl", see Fig. 1d-e, Table S1). The Pacific cold tongue warms more rapidly than the Pacific Warm Pool under 4×CO_2. In contrast, in G1 a more rapid cooling occurs in the Pacific Warm Pool and the SPCZ than in the cold tongue. The Pacific Warm Pool is ~0.4-0.6 ^{o}C colder in G1 than in piControl whereas the East Pacific cools less (~-0.2 ^{o}C in the Niño3 region).

Our SST results under 4xCO_2 agree with previous studies (Liu et al., 2005; van Oldenborgh et al., 2005; Collins et al., 2010; Vecchi and Wittenberg et al., 2010; Cai et al., 2015a; Huang and Ying et al., 2015; Luo et al., 2015; Kohyama et al., 2017; Nowack et al., 2017) that indicated an El Niño like mean state response to increased GHG concentration scenarios in the tropical Pacific. Overcooling of the tropics (and as such the tropical Pacific) is also a robust signal in G1 simulations, even short ones, simply due to the different meridional distribution of shortwave and longwave forcing (Govindasamy and Caldeira 2000; Lunt et al., 2008; Kravitz et al., 2013b; Curry et al., 2014; Nowack et al., 2016). The results presented here based on a long simulation not only confirm previously published results but also statistically demonstrate that under G1, the warm pool and SPCZ cools faster than the cold tongue.

3.1.2 Precipitation

In the tropical Pacific there are three dominant bands of rainfall activity: one in the western Pacific Warm Pool, one in the SPCZ, and the last one is part of the ITCZ situated over 8^{o} N and 150^{o} W-90^{o} W. The eastern equatorial Pacific is relatively dry compared with these three rainy bands. In piControl, HadCM3L simulates well these rainfall spatial patterns, with maxima of ~6-8, ~12-14, and ~8-10 mm day^{-1} over the Pacific Warm Pool, the SPCZ, and the northern part of the ITCZ, respectively (Fig. 2a). Under 4×CO_2, the rainfall spatial pattern changes significantly. The ITCZ moves equatorward and the SPCZ becomes zonally oriented (green line, Fig. 2b). The rainfall asymmetry between the western and eastern equatorial Pacific decreases under 4×CO_2. Precipitations migrate from the western Pacific to the Niño3 region, with maximum rainfall at ~145^{o} W. The reduced zonal asymmetry in rainfall between western and eastern Pacific is effectively restored to preindustrial state in G1 (Fig. 2c).

A statistically significant (99 % cl) overall precipitation increase of 0.21 mm day^{-1} (+5 %) is observed over the tropical Pacific under 4×CO_2 (Fig. 2d). In contrast, the mean rainfall in G1 decreases by 0.23 mm day^{-1} (-5 %; Fig. 2e), consistent with the simulated decrease of temperature (-0.30 ^{o}C) over the tropical Pacific. However, there is a strong regional structure: under 4×CO_2, rainfall decreases to a maximum of ~3 mm day^{-1} over parts of the Pacific Warm Pool and off-equatorial regions, whereas a significant increase of ~15-18 mm day^{-1} is observed over the Niño3 region. In G1 rainfall decreases over the Pacific Warm Pool, SPCZ,

Atmos. Chem. Phys. Discuss., https://doi.org/10.5194/acp-2018-1312
Manuscript under review for journal Atmos. Chem. Phys.
Discussion started: 7 January 2019

and ITCZ regions, whereas rainfall increases significantly over most parts of central and eastern equatorial Pacific, with a maximum (~ 1.5-2 mm day^{-1}) centered at ~150° W (Fig. 2e).

The position of the ITCZ over the tropical Pacific (25° N-25° S; 90° E-60° W) is calculated by finding the latitude of maximum rainfall (green lines, Fig. 2a-c). In piControl, the median position of this maximum ITCZ (from 154° W-82° W) north of the equator is 7.5° N, 0°, and 7.5° N under piControl, 4×CO_2 and G1, respectively. Under 4×CO_2, the ITCZ moves 7.5° southward (Fig. S1). Thus, under 4×CO_2, the ITCZ mean position moves over the equator and is positioned within the Niño3 region. G1 restores the ITCZ and SPCZ to their preindustrial orientations but differences in the magnitude of rainfall persist over these regions, as well as over the Pacific Warm Pool (Fig. 2a, c, e). That is, while the problem of reduced rainfall asymmetry between the western and eastern Pacific in 4×CO_2 is largely resolved in G1, the tropical Pacific is overall wetter under 4×CO_2 but drier in G1.

3.1.3 Zonal wind stress

Changes in zonal wind stress are directly dependent on and interacting with ENSO amplitude (Guilyardi 2006), ENSO period (Zelle et al., 2005; Capotondi et al., 2006), and ZSSTG (Hu and Fedorov 2016). A positive feedback loop between zonal wind stress, SST, and thermocline depth influences the development of ENSO (Philip and van Oldenborgh 2006). A decrease in the strength of the trade winds is concurrent with a flattening of the thermocline, a reduction of upwelling in the eastern Pacific and increased SST in the eastern relative to the western equatorial Pacific, thus resulting in further weakening of the trade winds (Collins et al., 2010).

We use the zonal wind stress index, Westerly Wind Bursts (WWBs), and Easterly Wind Bursts (EWBs) to study the wind stress over the tropical Pacific. The zonal wind stress index is defined as the wind stress averaged over the equatorial tropical Pacific (5° N-5° S; 120° E-80° W), whereas selecting only the positive (negative) values of the wind stress over the same region defines the WWBs (EWBs) (Hu and Fedorov 2016). In the present study, the zonal wind stress is significantly reduced over most parts of the tropical Pacific, especially over the Niño3 region in both 4×CO_2 and G1 (Fig. 3a-e), in agreement with the altered zonal SST gradients in both scenarios (Fig. 1). The zonal wind stress weakens by 31 % and 10 % in 4×CO_2 and G1 (99 % cl) (Fig. 4a). The weakening in 4×CO_2 is compensated to some degree in G1 but the wind field does not recover completely to its preindustrial state. We also observe significant weakening of zonal wind stress over the Niño3 region both under 4×CO_2 and G1.

The strength of WWBs increases by 13 % under G1 relative to piControl (99 % cl), while the EWBs decrease in strength by 7 %. The strong WWBs are more closely linked to positive SST anomalies than negative SST anomalies (Cai et al., 2015a) and thus likely to result in an increase in frequency of extreme El Niño events (Hu and Fedorov 2016) in G1. The strength of both the WWBs and EWBs are reduced (99 % cl) under 4×CO_2, by 33 % and 28 %, respectively.

These findings in the 4×CO_2 simulation agree with Philip and van Oldenborgh (2006), who, in several climate models, found up to 40 % reduction in zonal wind stress in the 23rd century.

3.1.4 Zonal and meridional sea surface temperature gradients

The ZSSTG between western and eastern equatorial Pacific is one of its characteristic features. The ZSSTG is weak during an El Niño and strong during La Niña events (Latif et al., 2009). The ZSSTG is calculated as the difference between SST in the western Pacific Warm Pool (5° N-5° S; 100° E-126° E) and eastern equatorial Pacific (Niño3 region: 5° N-5° S; 160° E-150° W). The zonal SST gradient is reduced in 4xCO_2 and also in G1 (Fig. 4b) but the reduction relative to piControl is less in G1 (11 %) than in 4xCO2 (62 %).

The reduced zonal SST asymmetry in 4×CO_2 and G1 is consistent with the weakening of the trade winds and zonal wind stress as noted in Sect. 3.1.3. The weakening of trade winds can result in reduced upwelling in the eastern equatorial Pacific, and east to west surface currents (Collins et al., 2010), leading to an increase in El Niño events.

MSSTG is calculated as the SST averaged over the off-equatorial region (5° N-10° N; 150° W-90° W) minus SST averaged over the equatorial region (2.5° N-2.5° S; 150° W-90° W) (Cai et al., 2014). Reversal of sign or weakening of the MSSTG has been observed during extreme El Niño events as the ITCZ moves over the equator. Overall there is a change in sign and reduction of MSSTG both in 4×CO_2 (~-111 %,), and G1 (~-9 %) (99 % cl, Fig. S2 and Table S2). The decrease in strength of MSSTG is an indication that extreme El Niño events increase (Cai et al., 2014) under solar geoengineering.

Wang et al. (2017) observed a weakening of the MSSTG in a multi-model ensemble under RCP2.6, however they did not find any evidence of change in the ZSSTG in RCP2.6 and RCP8.5.

3.1.5 Thermocline depth

Previous studies (Vecchi and Soden 2007; Yeh et al., 2009) showed shoaling as well as reduction in the east-west tilt of the equatorial Pacific thermocline under increased GHG scenarios. A decrease in thermocline depth and slope is a dynamical response to reduced zonal wind stress. Shoaling of the equatorial Pacific thermocline can result in positive SST anomalies in the eastern equatorial Pacific and that can affect formation of El Niño (Collins et al., 2010).

Thermocline depth here is defined as the depth of 20 °C (for piControl and G1) and 24 °C (for 4×CO2) isotherms averaged between 5° N and 5° S, following Phillip and van Oldenborgh (2006). Due to surface warming in GHG scenarios, the 20 °C isotherm deepens (Yang and Wang et al., 2009) and this must be compensated by using a warmer isotherm (24 °C) as a metric in the 4×CO2 case.

In 4xCO_2, the tropical Pacific thermocline depth (24 °C isotherm) shoals by 22 % (Fig. 4c), as expected from similar experiments (Vecchi and Soden 2007; Yeh et al., 2009). However, there is no statistically significant change in the mean thermocline depth in G1. Sun shading completely offsets shoaling of the thermocline depth which is characteristic of GHG warming scenarios.

3.1.6 Vertical velocity and Walker circulation

Under normal conditions, in the tropical Pacific, there is strong atmospheric upwelling over the western equatorial Pacific, SPCZ, and that part of the ITCZ located north of the equatorial tropical Pacific, whereas the relatively cold and dry eastern Pacific is dominated by atmospheric downwelling. This process, as simulated in HadCM3L, can be clearly seen in maps of Omega500-100 in Fig. 5a. The region of ascent over the SPCZ and ITCZ moves equatorward in 4×CO_2 (Fig 5b), consistent with the increase in SST and precipitation over the equatorial region (Fig. 1d and 2d). In 4×CO_2, the convective center also moves towards the Niño3 region centered at ~150^{o}W. These changes are largely offset in G1, which indicates that decreasing the downward shortwave flux can largely steer these atmospheric changes back to preindustrial state (Fig. 5c).

While spatial patterns in atmospheric divergence and convergence can be corrected in G1 (Fig. 5c), important differences remain. These are mostly associated with the magnitude of atmospheric convection. Specifically, a significant decrease in strength of upwelling is observed over the warm pool, while an increase is seen in the central pacific and the eastern part of Niño3 region (Fig. 5d-e); this happens both for 4×CO_2 and G1. The downwelling becomes weaker (i.e. less positive in Fig. 5e) in G1 over most parts of the eastern equatorial Pacific and over South America.

These changes are consistent with changes in the spatial extent and strength of the tropical PWC in 4×CO_2 and G1 (Fig. 6a-c). In 4×CO_2, the time-averaged western branch of the PWC extends further eastward and becomes broader, in agreement with the changes in Omega500-100 described above, while the eastern branch of the PWC is squeezed. The PWC reverts back to preindustrial spatial patterns in G1 (Fig. 6c).

Significant (90 % cl) changes occur in the strength of the PWC in 4×CO_2 and G1 relative to piControl (Fig. 6d-e). Both the western and eastern branches of the PWC become weaker in strength, whereas the vertical velocity strengthens in the central Pacific. Thus, G1 offsets the changes in spatial pattern of PWC occurring under increased GHG forcing but fails to completely compensate changes in strength.

3.2 ENSO amplitude and frequency

In Sect. 3.1 we noted significant changes in the tropical Pacific mean state, such as weakening of zonal and meridional SST gradients, zonal wind stress, and PWC. These changes can affect the ENSO variability. In this section, we discuss various metrics used to characterise ENSO variability and show how they change in 4xCO_2 and G1. Specifically, we investigate the amplitude of ENSO, changes in amplitude asymmetry between El Niño and La Niña events, and ENSO frequency.

3.2.1 ENSO amplitude

Three ENSO indices (Niño3, Niño4, and Niño3.4) are used to characterize changes in ENSO. All three indices are necessary because extreme warm and cold events are not simply mirror images of each other (Cai et al., 2015b). ENSO amplitude is defined as the standard deviation of SST anomalies in a given ENSO region (e.g., Philip and van Oldenborgh 2006; Nowack et al., 2017). The maximum amplitude of warm events is defined as the maximum positive ENSO anomaly during the entire time series analysed (Gabriel and Robock 2015). Cold events are defined similarly, but using the maximum negative ENSO anomaly.

In 4×CO_2, all ENSO indices show a decrease (47-64 %), whereas in G1, Niño3 and Niño3.4 indices show an increase (5-8 %) in amplitude at 99 % cl (Table 1). Further, in 4×CO_2, all ENSO indices show a decrease in the maximum amplitude of warm (30-57 %) and cold (19-36 %) events (Table 2-3). In G1, Niño4 and Niño3.4 indices indicate a decrease (7-11 %) in maximum amplitude of warm events but only the Niño4 index indicates an increase (20 %) in maximum amplitude of cold events. Thus, owing to an overall strengthening of ENSO amplitude, and strengthening (weakening) of the maximum amplitude of cold (warm) events, our simulations imply that significant changes in ENSO events under solar geoengineering could occur despite global mean surface temperatures being very similar in G1 and preindustrial conditions.

In general, the El Niño events are stronger than La Niña events, and amplitudes of El Niño and La Niña events are asymmetric (An and Jin 2004; Schopf and Burgman 2006; Ohba and Ueda 2009; Ham 2017). In the present study, the strengthening (weakening) of maximum amplitude of cold (warm) events indicates that asymmetry of cold and warm event's amplitude would change in both 4×CO_2 and G1. The relative strength of ENSO warm and cold events can be measured by the skewness of SST over the ENSO regions (Vega-Westhoff and Sriver 2017). Following Ham (2017), we investigate the asymmetry of amplitude of El Niño and La Niña events by comparing the skewness of detrended Niño3 SST anomalies in piControl with 4×CO_2 and G1.

We find that, relative to piControl, the Niño3 SST skewness is reduced (at 99 % cl) by 190 %, in 4×CO_2 and by 65 % in G1 (Table 4). This is further illustrated in maps showing differences in skewness between 4×CO_2 and G1 with piControl (Fig. S3). Over the eastern equatorial Pacific, the SSTs are transformed from positively to negatively skewed under 4×CO_2 (Fig. S3). In G1, the skewness of SSTs is reduced over the entire equatorial Pacific. Thus, due to the concurrent strengthening of the maximum amplitude of cold events and weakening of warm events, and reduction in asymmetry of SST skewness, the intensity of cold events is predicted to increase compared to warm events under solar geoengineering.

Vega-Westhoff and Sriver (2017) also found a decrease in strength of ENSO amplitude in the RCP8.5 scenario in the Community Earth System Model (CESM). Our results also agree with Ham (2017) who found a 40 % reduction in ENSO amplitude asymmetry using several CMIP5 models in the RCP4.5 scenario.

3.2.2 El Niño frequency

We chose a threshold value of rainfall for defining extreme El Niño events based on the work of Cai et al., (2014), who chose averaged DJF Niño3 total rainfall exceeding 5 mm day^{-1} for this threshold based on observations. Cai et al., (2017) pointed out that the trend in Niño3 rainfall is contributed by two main factors: (1) the change in mean state of the tropical Pacific and (2) the change in frequency of extreme El Niño events. In studying the extremes only, the trend contributed by mean state changes should be subtracted from the raw time series. Hence, we fit a quadratic trend to the time series of rainfall data from which all extreme El Niño events (DJF total rainfall > 5 mm day^{-1}) have been excluded and then subtract this trend from the raw Niño3 rainfall time series.

Using the detrended time series, 8 moderate and 2 extreme El Niño events can be identified from the historical record between 1979 and 2017 (Fig. 7a). The MSSTG is negative during the 1982 and 1997 extreme events. The identification of extreme events is slightly sensitive to the choice of threshold. For example, a threshold of detrended Niño3 total rainfall of 5 mm day^{-1} does not recognize 2015 as an extreme El Niño year, since it has weak positive MSSTG. We repeat the same method with averaged DJF Niño3 rainfall anomalies greater the 3- and 4- mm day^{-1}. Rainfall anomaly of 3 mm day^{-1} identifies 2015 as an extreme El Niño year whereas 4 mm day^{-1} does not (Fig. 7b). Since, a threshold of total rainfall > 5 mm day^{-1} does not recognize El Niño events having weak positive MSSTG as extreme El Niño events, we use all three threshold values (total rainfall > 5 mm day^{-1}; and 3 and 4 mm day^{-1} rainfall anomaly) for detecting any change in extreme El Niño events under solar geoengineering experiment. Note that under piControl, total rainfall of 5 mm day^{-1} is ~95th percentile, whereas 4- (3-) mm day^{-1} anomaly is ~94th (~90th) percentile in detrended Niño3 rainfall time series.

Since there exists a nonlinear relationship between SST and Niño3 rainfall, for this method to be applicable the Niño3 rainfall skewness should be at least +1 (see Cai et al., 2014). Further, the skewness criterion is used to avoid climate models simulating overly wet or dry conditions over the Niño3 region (Cai et al., 2017). HadCM3L simulates skewness of 2.06, -0.07, and 1.55 for piControl, 4×CO_2, and G1, respectively. The reduced skewness of Niño3 rainfall under GHG forced climate indicates that nonlinear relationship between Niño3 rainfall and MSSTG completely breakdowns under 4×CO_2. Below, we only focus our analysis on G1 for studying the changes in ENSO extremes.

With detrended Niño3 total rainfall exceeding 5 mm day^{-1} as an extreme, a statistically significant (99 % cl) increase of 44 % in extreme El Niño events is observed under G1 (65 events) relative to piControl (45 events) (Fig. 7c-d). Thus, an extreme El Niño event occurring every ~22-yr under preindustrial conditions occurs every ~15-yr under solar geoengineered conditions. The moderate El Niño events increase by 7 % under G1, however, the change is not statistically significant. A statistically significant (95 %) increase of 12 % in frequency of total number of El Nino events (number of extreme plus moderate events) is also observed with number of events increasing from 300 in piControl to 337 in G1. Thus, an

El Niño event occurring every ~3.3-yr under preindustrial conditions occurs every ~2.9-yr under solar geoengineered conditions.

Results similar to those with 5 mm day^{-1} are found when using detrended Niño3 rainfall anomaly of 3 and 4 mm day^{-1} as definition thresholds for extreme El Niño events. Specifically, the number of extreme events increase by ~40 % and ~42 % for Niño3 rainfall anomaly thresholds of 3 and 4 mm day^{-1} respectively, and the frequency of total (extreme plus moderate) events increase by ~12 % in both cases in G1 relative to piControl (Fig. S4a-d).

No statistically significant changes in the number of extreme El Niño events is detected when using ENSO indices based on SST. However, all SST based ENSO indices (Niño3, Niño4, and Niño3.4) indicate statistically significant increase of ~12 % in frequency of total (extreme plus moderate) number of El Niño events (ENSO index > 0.5 s.d.) (Table S4).

There is no evidence of changes in the frequency of central Pacific El Niño (El Niño Modoki) comparative to the frequency of eastern Pacific El Niño (canonical El Niño) in G1 relative to piControl (not shown).

We note that under solar geoengineered climate, more weak and reversed MSSTG events occur relative to piControl (Fig. S2). More frequent reversals of MSSTG result into more frequent establishment of strong convection in the eastern equatorial Pacific. According to Cai et al. (2014), more frequent convection over the eastern tropical Pacific increases the sensitivity of rainfall by 25 % to positive SST anomalies. Further, in Sect. 3.1.3 we observed that WWBs (EWBs) are 13 % (7 %) stronger (weaker) than in piControl which also favors a higher frequency of El Niño events. Thus, we conclude that changes in the tropical Pacific mean state, in particular weakening of temperature gradients (MSSTG and ZSSTG), changes in zonal wind stress, and convection over the tropical Pacific (and consistent weakening of the PWC) are the possible causes of increased frequency of extreme El Niño events under G1.

3.2.3 La Niña frequency

During La Niña events, the ZSSTG, the PWC and atmospheric convection in the western Pacific are stronger than normal. Here, we present plots of Niño4 vs ZSSTG for piControl and G1 (Fig. 7e-f). We observe a statistically significant (95 % cl) increase in extreme La Niña events in the G1 experiment. The number of extreme La Niña events increases by 32 % (61 events) in G1 relative to piControl (46 events). Thus, an extreme La Niña event occurring every ~22-yr in piControl occurs every ~16-yr in G1. The other two ENSO indices (Niño3 and Niño3.4) also show statistically significant increases in extreme La Niña events in G1 (Table S5). The Niño3 (Niño3.4) shows ~400 % (~138 %) increase in extreme La Niña, meaning an extreme event occurring every ~124 (~62) years over the Niño3 (Niño 3.4) region in piControl occurs every ~25 (~26) years in G1. Increased number of extreme El Niño events results in more heat discharge events causing cooling, hence providing conducive conditions for increased occurrence of La Niña events (Cai et al., 2015a, 2015b).

3.3 Spatial characteristics of ENSO

Sect. 3.2 showed that the maximum amplitude of cold (warm) events is strengthened (weakened) and that the amplitude asymmetry between warm and cold events is significantly reduced in G1 relative to piControl. Here we provide process-based evidence for the strengthening (weakening) of extreme La Niña (El Niño) events in G1 relative to piControl. Using composite analysis, we show that for extreme La Niña (El Niño) events the PWC, SST and rainfall anomalies are strengthened in G1 relative to piControl. The composite anomalies are shown for the extreme and the total (extreme plus moderate) number of La Niña (El Niño) events in piControl and G1. We also calculate differences of composite anomalies between G1 and piControl (G1-piControl) to detect any significant change in ENSO characteristics under solar geoengineering.

3.3.1 El Niño composites

The spatial pattern of composite SST anomalies for extreme and total number of El Niño events in G1 is very similar to that of piControl with stronger warm anomalies in the eastern equatorial Pacific than in the off-equatorial and western Pacific region (Fig. 8a-d). However, the extreme El Niño composite difference (G1-piControl) indicates that warm anomalies over western, central, and eastern equatorial Pacific are weaker in G1 (Fig. 8e). The composite difference of total El Niño events also indicates statistically significant (90 % cl) weak warm anomalies over western and, central equatorial Pacific in G1 (Fig. 8f). Thus, in general, El Niño events tend to be weaker in G1 than in piControl.

The spatial pattern of composite rainfall anomalies for extreme and total El Niño events is alike both in G1 and piControl with peak positive rainfall anomalies centering at ~145^{o} W and ~160^{o} W, respectively (Fig. 9a-d). However, during extreme El Niño events, in accordance with weak warm SST anomalies over western, central, and eastern equatorial Pacific (Fig. 8e), the positive rainfall anomalies are also weaker (Fig. 9e). The composite difference for total El Niño events also indicates weaker positive rainfall anomalies over the central Pacific (Fig. 9f).

During El Niño events, the PWC reverses in sign and direction with stronger atmospheric upwelling over the eastern Pacific and downwelling over the western Pacific. The spatial patterns of PWC for the extreme and total number of El Niño events are similar both under G1 and piControl (Fig. 10a-d). During extreme (total number of) El Niño events the upwelling is centered at ~145^{o} W (~160^{o} W) both in G1 and piControl. In G1 relative to piControl, the atmospheric upwelling (downwelling) becomes weak over eastern (western) equatorial Pacific during extreme El Niño events (Fig. 10e) which agrees with reduced SST and rainfall anomalies over these regions (see Fig. 8e and 9e). For total El Niño events, in contrast to extreme El Niño events, the deep convection between 600 and 200 hPa over eastern Pacific is strengthened under G1 relative to piControl whereas the atmospheric downwelling becomes weak over western Pacific (Fig. 10f). Thus, during extreme El Niño events the PWC is weaker in G1 than in piControl.

We conclude that extreme El Niño events are more frequent but slightly less powerful in a solar geoengineered climate than in preindustrial conditions. We further confirm this with a histogram of detrended Niño3 SST anomalies (Fig. S5a). Though more frequent positive Niño3 SST anomalies occur under G1 (between 1.5 and 2.5 °C) the mean Niño3 SST anomaly is weaker in G1 (2.38 °C) than in piControl (2.16 °C) at 99 % cl. Thus, the strength of extreme El Niño events is reduced by ~9 % in G1 compared to piControl. However, no statistically significant shift in histograms of Niño3 SST anomalies is detected for the total number of El Niño events (Fig. S5b).

3.3.2 La Niña composites

The composite spatial patterns of SST, and the rainfall anomalies, for extreme and total number of La Niña events are similar under G1 and piControl (Fig 11a-d and Fig. 12a-d). During extreme La Niña events, the negative SST anomalies are stronger and more stretched towards western Pacific than that for the total La Niña events. The peak negative rainfall anomalies occur in the Niño4 region for both for extreme and total La Niña events composites. The composite differences of SSTs (Fig. 11e-f) and rainfall (Fig. 12e-f) anomalies for both extreme and total La Niña events show that negative SST and rainfall anomalies are stronger in G1 than in piControl. Thus, under G1 the extreme and total events are stronger than in piControl. These composite differences also show that during extreme and total La Niña events, the western Pacific and western coast of south America is warmer and wetter under G1 compared to piControl.

The PWC is strengthened during La Niña events. The spatial pattern of composite PWC for extreme and total La Niña events is similar both under G1 and piControl (Fig. 13a-d). However, the composite differences indicate that PWC is stronger in G1 than in piControl both for extreme and total La Niña events (Fig. 13e-f) consistent with stronger negative SST and rainfall anomalies in the eastern and central equatorial Pacific.

We note that stronger negative SST anomalies occur over the eastern equatorial Pacific under G1 compared to piControl indicating an overall increase in strength of La Niña events in solar geoengineered climate (Fig. 11e-f). We further confirm this with histograms of detrended Niño3 SST anomalies for extreme and total number of La Niña events based on the Niño4 SST index (Fig. S5c-d). Figures S5c-d clearly show that under G1 compared to piControl stronger negative SST anomalies occur over eastern equatorial Pacific during the extreme (piControl: -1.45 °C; G1: -1.68 °C) and the total number of La Niña events (piControl: -1.03 °C; G1: -1.22 °C). Thus, we conclude that the strength of extreme (total number of) La Niña events is increased by ~16 % (~18 %) in G1 compared to piControl.

4 Discussion and conclusions

In this paper we have analysed the impact of increased GHG forcing (4×CO_2) and solar geoengineering (G1) on the tropical Pacific mean climate and ENSO extremes. Previous solar geoengineering studies did not show any statistically significant change in the PWC (e.g., Guo et al., 2018) or ENSO frequency and amplitude (e.g., Gabriel and Robock 2015). However, those results were strongly limited by the length of the respective GeoMIP simulations, which made changes difficult to detect given the high climate tropical Pacific climate variability. This problem was overcome here by using long (1000 years) climate model simulations, carried out with HadCM3L. The longer record makes it possible to detect small changes between the preindustrial and G1 scenarios within the chosen model system.

We find that manipulating the downward shortwave flux through solar geoengineering can compensate some of the greenhouse-induced changes in the tropical Pacific but not all. Importantly, manipulating the downward shortwave flux cannot correct one of the climate system's most dominant mode of variability, ENSO, back to preindustrial conditions. Specifically, we find that:

1. The warming over the tropical Pacific under increased GHG forcing (4×CO_2) is overcompensated under solar sunshade (G1) geoengineering resulting, by design, in a cooling of 0.3 ^oC. This overcooling is more pronounced in the western tropical Pacific and SPCZ than in the eastern Pacific under the G1 scenario. This shows that even in an ideal situation, where shading is applied as soon as GHG forcing is introduced, the climate will experience changes in regional gradients. The implication is that solar engineering experiments could benefit from applying spatially variable shadings to redress some of the changes induced by the GHGs.
2. The reduced SST and rainfall asymmetry, between the warm pool and the cold tongue, observed under 4×CO_2, is mostly corrected in G1, but regionally important differences remain relative to preindustrial conditions. The tropical Pacific is 5 % wetter in 4×CO_2 whereas 5 % drier in G1 relative to piControl. Solar geoengineering results in decreased rainfall over the warm pool, SPCZ, and ITCZ and an increase over the central and eastern equatorial Pacific.
3. The preindustrial median position of ITCZ north of the equator (154^o W-82^o W; 7.5^o N) changes significantly under 4×CO_2 and moves over the equator (154^o W-82^o W; 0^o). G1 restores the ITCZ to its preindustrial position (154^o W-82^o W; 7.5^o N).
4. The increased GHG forcing results in 31 % reduction in zonal wind stress over the tropical Pacific. G1 fails to completely compensate this reduction, and results in weakening the zonal wind stress by 10 % with 13 % (7 %) increase (decrease) in WWBs (EWBs), thus providing more conducive conditions for El Niño extremes.
5. Under solar geoengineering, both ZSSTG and MSSTG are reduced by 11 % and 9 %, respectively. More frequent reversal of MSSTG occurs in G1 relative to piControl.
6. In 4×CO_2, the thermocline shoals by 22 % over the tropical Pacific, however G1 completely recovers it to its preindustrial orientation.
7. The PWC becomes weaker both under 4×CO_2 and G1 scenarios.
8. The increased GHG forcing results in weakening of ENSO amplitude by 30-57 % whereas solar geoengineering strengthens it by 5-8 % relative to preindustrial. The maximum amplitude of warm (cold) events is reduced (increased) under G1.
9. The ENSO amplitude asymmetry between warm and cold events is reduced under G1 relative to piControl.
10. The frequency of extreme El Niño events increases by 44 % in G1 relative to piControl. Hence, an extreme El Niño event occurring every ~22-yr under

preindustrial conditions occurs every ~15-yr under solar geoengineered conditions. Further, the frequency of total number (extreme plus moderate) of El Niño events also increases by 12 %. Thus, an El Niño event occurring every ~3.3-yr under preindustrial conditions occurs every ~2.9-yr under solar geoengineered climate. The reason for occurrence of more extreme El Niño events under G1 is more frequent reversals of MSSTG compared to piControl.

11. The frequency of extreme La Niña events increases by 32 % under G1 relative to piControl. Thus, an extreme La Niña event occurring every ~22-yr in piControl occurs every ~16-yr in G1.
12. The extreme El Niño events are ~9 % weaker whereas all La Niña events are ~18 % stronger under G1 compared to piControl.

Author contribution. Long Cao developed the model code and performed the simulations. Abdul Malik formulated the research questions, defined the methodology with the help of all co-authors, and performed the scientific analysis. Abdul Malik prepared the manuscript with contributions from all co-authors.

Competing interests. The authors declare that they have no conflict of interest.

Data availability. Data are available upon request from Long Cao (longcao@zju.edu.cn).

Acknowledgments

This work was supported by the Swiss National Science Foundation under grant EarlyPostdoc.Mobility (P2BEP2_175255). GPCP Precipitation and NCEP Reanalysis data was provided by the NOAA/OAR/ESRL PSD, Boulder, Colorado, USA, from their Web site at https://www.esrl.noaa.gov/psd/. PJN is supported through an Imperial College Research Fellowship.

References

Adler, R. F., Huffman, G. J., Chang, A., Ferraro, R., Xie, P-P., Janowiak, J., Rudolf, B., Schneider, U., Curtis, S., Bolvin, D., Gruber, A., Susskind, J., Arkin, P., and Nelkin, E.: The version-2 Global Precipitation Climatology Project (GPCP) monthly precipitation analysis (1979–Present), J. Hydrometeorol., 4, 1147–1167, https://doi.org/10.1175/1525-7541(2003)004<1147:TVGPCP>2.0.CO;2, 2003.

An, S-II., and Jin, F-F.: Nonlinearity and Asymmetry of ENSO, J. Climate., 17, 2399–2412, https://doi.org/10.1175/1520-0442(2004)017<2399:NAAOE>2.0.CO;2, 2004.

Boer, G. J., Yu, B., Kim, S., and Flato, G. M.: Is there observational support for an El Niño-like pattern of future global warming?, Geophys. Res. Lett., 31, 1–4, https://doi.org/10.1029/2003GL018722, 2004.

Bove, M. C., Elsner, J. B., Landsea, C. W., Niu, X., O Brien, J. J.: Effect of El Niño on U.S. landfalling hurricanes, revisited, B. Am. Meteorol. Soc., 79 (11), 2477-2482, https://doi.org/10.1175/1520-0477(1998)079<2477:EOENOO>2.0.CO;2, 1998.

Cai, W., Borlace, S., Lengaigne, M., van Rensch, P., Collins, M., Vecchi, G., Timmermann, A., Santoso, A., McPhaden, M. J., Wu, L., England, M. H., Wang, G., Guilyardi, E., and Jin, F-F.: Increasing frequency of extreme El Niño events due to greenhouse warming, Nat. Clim. Change., 4(2), 111–116, https://doi.org/10.1038/nclimate2100, 2014.

Cai, W., Santoso, A., Wang, G., Yeh, S. W., An, S. Il, Cobb, K. M., Collins, M., Guilyardi, E., Jin, F-F., Kug, J-S., Lengaigne, M., McPhaden, M. J., Takahashi, K., Timmermann, A., Vecchi, G., Watanabe, M., and Wu, L.: ENSO and greenhouse warming. Nat. Clim. Change., 5(9), 849–859. https://doi.org/10.1038/nclimate2743, 2015a.

Cai, W., Wang, G., Santoso, A., Lin, X., and Wu, L.: Definition of Extreme El Niño and Its Impact on Projected Increase in Extreme El Niño Frequency. Geophys. Res. Lett., 44(21), 11184-11190, https://doi.org/10.1002/2017GL075635, 2017.

Cai, W., Wang, G., Santoso, A., Mcphaden, M. J., Wu, L., Jin, F-F., Timmermann, A., Collins, M., Vecchi, G., Lengaigne, M., England, M. H., Dommenget, D., Takahashi, K., and Guilyardi, E.: Increased frequency of extreme La Niña events under greenhouse warming, Nat. Clim. Change., 5(2), 132–137, https://doi.org/10.1038/nclimate2492, 2015b.

Cao, L., Duan, L., Bala, G., and Caldeira, K.: Simulated long-term climate response to idealized solar geoengineering, Geophys. Res. Lett., 43(5), 2209-2217, https://doi.org/10.1002/2016GL068079, 2016.

Capotondi, A., Wittenberg, A., Masina, S.: Spatial and temporal structure of Tropical Pacific interannual variability in 20th century coupled simulations, Ocean. Model., 15(3-4), 274-298, https://doi.org/10.1016/j.ocemod.2006.02.004, 2006.

Chen, L., Li, T., Yu, Y., and Behera, S. K.: A possible explanation for the divergent projection of ENSO amplitude change under global warming,, Clim. Dynam., 49(11–12), 3799–3811, https://doi.org/10.1007/s00382-017-3544-x, 2017.

Collins, M., Tett, S. F. B., and Cooper, C.: The internal climate variability of HadCM3, a version of the Hadley Centre coupled model without flux adjustments. Clim Dynam, 17(1), 61–81, https://doi.org/10.1007/s003820000094, 2001.

Collins, M., An, S.-I., Cai, W., Ganachaud, A., Guilyardi, E., Jin, F.-F., Jochum, M., Lengaigne, M., Power, S., Timmermann, A., Vecchi, G., and Wittenberg, A.: The impact of global warming on the tropical Pacific Ocean and El Niño. Nature Geoscience, 3(6), 391–397, https://doi.org/10.1038/ngeo868, 2010.

Cox, P. M., Betts, R. A., Jones, C. D., Spall, S. A., and Totterdell, I. J.: Acceleration of global warming due to carbon-cycle feedbacks in a coupled climate model, Nature, https://doi.org/10.1038/35041539, 2000.

Crutzen, P. J: Albedo enhancement by stratospheric sulfur injections: A contribution to resolve a policy dilemma?, Climatic Change, 77(3–4), 211–219, https://doi.org/10.1007/s10584-006-9101-y, 2006.

Curry, C. L., Sillmann, J., Bronaugh, D., Alterskjaer, K., Cole, J. N. S., Ji, D., Kravitz, B., Kristjánsson, J. E., Moore, J. C., Muri, H., Niemeier, U., Robock, A., Tilmes, S., and Yang, S.: A multimodel examination of climate extremes in an idealized geoengineering experiment, J. Geophys. Res-Atmos., 119(7), 3900–3923, https://doi.org/10.1002/2013JD020648, 2014.

Essery, R., and Clark, D. B.: Developments in the MOSES 2 land-surface model for PILPS 2e, Global Planet. Change., 38(1-2), 161–164,, https://doi.org/10.1016/S0921-8181(03)00026-2, 2003.

Gabriel, C. J., and Robock, A.: Stratospheric geoengineering impacts on El Niño/Southern Oscillation, Atmos. Chem. Phys., 15(20), 11949–11966, https://doi.org/10.5194/acp-15-11949-2015, 2015.

Gibbons, J. D., and Chakraborti, S., : Nonparametric Statistical Inference, 5th Ed., Statistics: Textbooks & Monographs, Chapman and Hall/CRC Press, Taylor and Francis Group, 2011

Govindasamy, B., Caldeira, K.: Geoengineering Earth's radiation balance to mitigate CO2-induced climate change, Geophys. Res. Lett., 27(14), 2141-2144, https://doi.org/10.1029/1999GL006086, 2000.

Guilyardi, E.: El Niño–mean state–seasonal cycle interactions in a multi-model ensemble, Clim. Dynam., 26(4), 329-348, https://doi.org/10.1007/s00382-005-0084-6 , 2006.

Guo, A., Moore, J. C., and Ji, D.: Tropical atmospheric circulation response to the G1 sunshade geoengineering radiative forcing experiment, Atmos. Chem. Phys., 18, 8689-8706, https://doi.org/10.5194/acp-18-8689-2018, 2018.

Ham, Y.: A reduction in the asymmetry of ENSO amplitude due to global warming: The role of atmospheric feedback, Geophys. Res. Lett., 44(16), 8576–8584, https://doi.org/10.1002/2017GL074842, 2017.

Hollander, M., and Wolfe D. A.: Nonparametric Statistical Methods, 2nd Ed., John Wiley and Sons, Inc., 1999.

Hong, Y., Moore J. C., Jevrejeva, S., Ji, D., Phipps, S. J., Lenton,, A., Tilmes, S., Watanabe, S., and Zhao, L.: Impact of the GeoMIP G1 sunshade geoengineering experiment on the Atlantic meridional overturning circulation, Environ. Res. Lett., 12(3), https://doi.org/10.1088/1748-9326/aa5fb8, 2017.

Hu, S., and Fedorov, A. V.: Exceptionally strong easterly wind burst stalling El Niño of 2014, P. Natl. Acad. Sci. USA., 113(8), 2005-2010, https://doi.org/10.1073/pnas.1514182113, 2016.

Huang, P., and Ying, J.: A multimodel ensemble pattern regression method to correct the tropical pacific SST change patterns under global warming. J. Climate., 28(12), 4706–4723, https://doi.org/10.1175/JCLI-D-14-00833.1, 2015.

Kim, S. T., Cai, W., Jin, F.-F., Santoso, A., Wu, L., Guilyardi, E., and An, S.-I.: Response of El Niño sea surface temperature variability to greenhouse warming. Nat. Clim. Change., 4(9), 786–790, https://doi.org/10.1038/nclimate2326, 2014.

Kohyama, T., Hartmann, D. L., and Battisti, D. S.: La Niña-like mean-state response to global warming and potential oceanic roles, J. Climate., 30(11), 4207–4225, https://doi.org/10.1175/JCLI-D-16-0441.1, 2017.

Kravitz, B., Caldeira, K., Boucher, O., Robock, A., Rasch, P. J., Alterskjær, K., Karam, D. B., Cole, J. N. S., Curry, C. L., Haywood, J. M., Irvine, P. J., Ji, D., Jones, A., Kristjánsson, J. E., Lunt D. J., Moore, J. C., Niemeier, U., Schmidt, H., Schulz, M., Singh, B., Tilmes, S., Watanabe, S., Yang, S., Yoon, J-H.: Climate model response from the Geoengineering Model Intercomparison Project (GeoMIP), J. Geophys. Res-Atmos., 118, 8320–8332, https://doi.org/10.1002/jgrd.50646, 2013b.

Kravitz, B., Forster, P. M., Jones, A., Robock, A., Alterskjær, K., Boucher, O., Jenkins, A. K. L., Korhonen, H., Kristjánsson, J. E., Muri H., Niemeier, U., Partanen, A-I., Rasch, P. J., Wang, H., Watanabe, S.: Sea spray geoengineering experiments in the geoengineering model intercomparison project (GeoMIP): Experimental design and preliminary results, J. Geophys. Res-Atmos., 118(19), 11175–11186, https://doi.org/10.1002/jgrd.50856, 2013a.

Kravitz, B., Robock, A., Boucher, O., Schmidt, H., Taylor, K. E., Stenchikov, G., and Schulz, M.: The Geoengineering Model Intercomparison Project (GeoMIP), Atmos. Sci. Lett., 12(2), 162–167, https://doi.org/10.1002/asl.316, 2011.

Latif, M., and Keenlyside, N. S.: El Niño/Southern Oscillation response to global warming, P. Natl. Acad. Sci. USA., 106 (49), 20578-20583, 10.1073/pnas.0710860105, 2009.

Liu, Z., Vavrus, S., He, F., Wen, N., and Zhong, Y.: Rethinking tropical ocean response to global warming: The enhanced equatorial warming. J. Climate., 18(22), 4684–4700, https://doi.org/10.1175/JCLI3579.1, 2005.

Lunt, D. J., Ridgwell, A, Valdes, P. J., Seale, A.: Sunshade World: A fully coupled GCM evaluation of the climatic impacts of geoengineering, Geophys. Res. Lett., 35(L12710), https://doi.org/10.1029/2008GL033674, 2008.

Luo, Y., Lu, J., Liu, F., and Liu, W.: Understanding the El Niño-like oceanic response in the tropical Pacific to global warming, Clim. Dynam., 45(7–8), 1945–1964, https://doi.org/10.1007/s00382-014-2448-2, 2015.

Malik, A., Brönnimann, S., Stickler, A., Raible, C. C., Muthers, S., Anet, J., Rozanov, E., Schmutz, W.: Decadal to multi-decadal scale variability of Indian summer monsoon rainfall in the coupled ocean-atmosphere-chemistry climate model SOCOL-MPIOM, Clim. Dynam., 49(9–10), 3551–3572, https://doi.org/10.1007/s00382-017-3529-9, 2017.

Meehl G. A., Washington, W. M.: El Niño like climate change in a model with increased atmospheric CO2 concentrations, Nature, 382, 1996.

Moore, T. R., Matthews, H. D., Simmons, C., and Leduc, M.: Quantifying changes in extreme weather events in response to warmer global temperature, Atmos. Ocean., 53(4), 412–425, https://doi.org/10.1080/07055900.2015.1077099, 2015.

Nowack, P. J., Abraham, N. L., Braesicke, P., and Pyle, J. A.: Stratospheric ozone changes under solar geoengineering: implications for UV exposure and air quality, Atmos. Chem. Phys., 16, 4191–4203, https://doi.org/10.5194/acpd-15-31973-2015, 2016.

Nowack, P. J., Abraham, N. L., Braesicke, P., and Pyle J. A.: The impact of stratospheric ozone feedbacks on climate sensitivity estimates, J. Geophys. Res. Atmos., 123, 4630–4641, https://doi.org/10.1002/2017JD027943, 2018.

Nowack, P. J., Abraham, N. L., Maycock, A. C., Braesicke, P., Gregory, J. M., Joshi, M. M., Osprey, A., and Pyle, J. A.: A large ozone-circulation feedback and its implications for global warming assessments, Nat. Clim. Chang., 5(1), 41–45, https://doi.org/10.1038/nclimate2451, 2015.

Nowack, P. J., Braesicke, P., Abraham, N. L., and Pyle J. A.: On the role of ozone feedback in the ENSO amplitude response under global warming, Geophys. Res. Lett., 44, 3858–3866, https://doi.org/10.1002/2016GL072418, 2017.

Ohba, M., Ueda H.: Role of nonlinear ntmospheric response to SST on the asymmetric transition process of ENSO, 177–192. https://doi.org/10.1175/2008JCLI2334.1, 2009.

Pachauri, R. K., Allen, M. R., Barros, V. R., Broome, J., Cramer, W., Christ, R., Church, J. A., Clarke, L., Dahe, Q., Dasgupta, P., Dubash, N. K., Edenhofer, O., Elgizouli, I., Field, C. B., Forster, P., Friedlingstein, P., Fuglestvedt, J., Gomez-Echeverri, L., Hallegatte, S., Hegerl, G., Howden, M., Jiang, K., Jimenez Cisneroz, B., Kattsov, V., Lee, H., Mach, K. J., Marotzke, J., Mastrandrea, M. D., Meyer, L., Minx, J., Mulugetta, Y., O'Brien, K., Oppenheimer, M., Pereira, J. J., Pichs-Madruga, R., Plattner, G. K., Pörtner, H. O., Power, S. B., Preston, B., Ravindranath, N. H., Reisinger, A., Riahi, K., Rusticucci, M., Scholes, R., Seyboth, K., Sokona, Y., Stavins, R., Stocker, T. F., Tschakert, P., van Vuuren, D., and van Ypserle, J. P.: Climate change 2014: synthesis report, contribution of Working Groups I, II and III to the Fifth Assessment Report of the Intergovernmental Panel on Climate Change, Pachauri, R., and Meyer, L., (Eds.) , Geneva, Switzerland, IPCC, 151 p., ISBN: 978-92-9169-143-2, 2014

Park, W., Keenlyside, N., Latif, M., Ströh, A., Redler, R., Roeckner, E., and Madec, G.: Tropical Pacific climate and its response to global warming in the Kiel Climate Model. J. Climate., 22(1), 71–92, https://doi.org/10.1175/2008JCLI2261.1, 2009.

Philip, S. Y., and van Oldenborgh, G. J.: Shifts in ENSO coupling processes under global warming, Geophys. Res. Lett., 33(11), 1–5, https://doi.org/10.1029/2006GL026196, 2006.

Rayner, N. A., Parker, D. E., Horton, E. B., Folland, C. K., Alexander, L. V, Rowell, D. P., … Kaplan, A.: Global analyses of sea surface temperature , sea ice , and night marine air temperature since the late nineteenth century, J. Geophys. Res-Atmos., 108(D14), https://doi.org/10.1029/2002JD002670, 2003.

Ropelewski, C. F., and Halpert, M. S.: Global and regional scale precipitation patterns associated with the El Niño/Southern Oscillation, Mon Weather Rev., https://doi.org/10.1175/1520-0493(1987)115<1606:GARSPP>2.0.CO;2, 1987.

Santoso, A., Mcphaden, M. J., and Cai, W.: The defining characteristics of ENSO extremes and the strong 2015/2016 El Niño, Rev. Geophys., 55(4), 1079–1129, https://doi.org/10.1002/2017RG000560, 2017.

Schmidt, H., Alterskjær, K., Alterskjær, K., Bou Karam, D., Boucher, O., Jones, A., … Timmreck, C.: Solar irradiance reduction to counteract radiative forcing from a quadrupling of CO2: Climate responses simulated by four earth system models, Earth. Syst. Dynam., 3(1), 63–78, https://doi.org/10.5194/esd-3-63-2012, 2012.

Schopf, P. S., and Burgman R. J.: A simple mechanism for ENSO residuals and asymmetry, J. Climate., 19, 3167–3179, 2006.

Stevenson, S., Fox-Kemper, B.: ENSO model validation using wavelet probability analysis, J. Climate., 23, 5540–5547, https://doi.org/10.1175/2010JCLI3609.1, 2010.

Stocker T. F., Qin D., Plattner, G. K., Tignor M., Allen, S. K., Boschung, J., Nauels, A., Xia, Y., Bex, V., Midgley P. M. (Eds.): Summary for Policymakers, in: Climate Change 2013: The Physical Science Basis. Contribution of Working Group I to the Fifth Assessment Report of the Intergovernmental Panel on Climate Change, Cambridge University Press, Cambridge, UK and New York, NY, USA, https://doi.org/10.1017/CBO9781107415324.004, 2013.

van Oldenborgh, G. J., Philip, S. Y., and Collins, M.: El Niño in a changing climate: A multi-model study, Ocean. Sci., 1(2), 81–95, https://doi.org/10.5194/os-1-81-2005, 2005.

Vecchi G. A., Soden B. J., (2007). Global warming and the weakening of the tropical circulation, J. Climate., 20, 4316–4340, https://doi.org/10.1175/JCLI4258.1, 2007.

Vecchi, G. A., Soden, B. J., Wittenberg, A. T., Held, I. M., Leetmaa, A., and Harrison, M. J: Weakening of tropical Pacific atmospheric circulation due to anthropogenic forcing, Nature, 441, 73–76, https://doi.org/10.1038/nature0474, 2006.

Vecchi, G. A., and Wittenberg, A. T.: El Niño and our future climate: where do we stand? Wiley Interdiscip. Rev. Clim. Chang., 1(2), 260–270, https://doi.org/10.1002/wcc.33, 2010.

Vega-Westhoff, B., and Sriver, R. L: Analysis of ENSO's response to unforced variability and anthropogenic forcing using CESM, Scientific Reports, 7(1), 1–10, https://doi.org/10.1038/s41598-017-18459-8, 2017.

Wang, G., Cai, W., Gan, B., Wu, L., Santoso, A., Lin, X., Chen, Z., and McPhaden, M. J.: Continued increase of extreme El Ninõ frequency long after 1.5 C warming stabilization, Nat. Clim. Change., 7(8), 568–572, https://doi.org/10.1038/NCLIMATE3351, 2017.

Wang, Y., Luo, Y., Lu, J., and Liu, F.: Changes in ENSO amplitude under climate warming and cooling, Clim. Dynam., 53–53. https://doi.org/10.1007/s00382-018-4224-1, 2018.

Wigley, T., M., L.: A combined mitigation/geoengineering approach to climate stabilization, Science, 314(5798), 452-454, 10.1126/science.1131728, 2006.

Yang, H., Wang F.: Revisiting the thermocline depth in the equatorial Pacific, J. Climate., 22, 3856–3863, https://doi.org/10.1175/2009JCLI2836.1, 2009.

Yang, S., Li, Z., Yu, J.-Y., Hu, X., Dong, W., and He, S.: El Niño–Southern oscillation and its impact in the changing climate, Natl Sci Rev, nwy046, https://doi.org/10.1093/nsr/nwy046, 2018.

Yeh, S. W., Kug, J. S., Dewitte, B., Kwon, M. H., Kirtman, B. P., and Jin, F. F; El Niño in a changing climate, Nature, 461(7263), 511–514, https://doi.org/10.1038/nature08316, 2009.

Zelle, H., van Oldenborgh, G. J., Burgers, G., and Dijkstra, H.: El Niño and greenhouse warming: results from ensemble simulations with the NCAR CCSM, J. Climate., 18, 4669-4683, https://doi.org/10.1175/JCLI3574.1, 2005.

Zhou, Z. Q., and Xie, S. P: Effects of climatological model biases on the projection of tropical climate change, J. Climate., 28(24), 9909–9917, https://doi.org/10.1175/JCLI-D-15-0243.1, 2015.

Atmos. Chem. Phys. Discuss., https://doi.org/10.5194/acp-2018-1312
Manuscript under review for journal Atmos. Chem. Phys.
Discussion started: 7 January 2019

Figures and Figure Captions

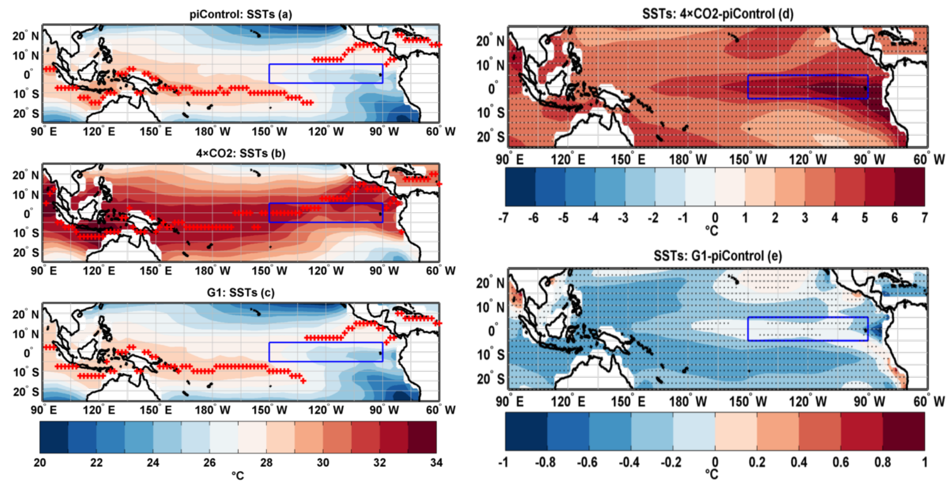

Figure 1. Tropical Pacific SST mean DJF climatology (a) piControl (b) 4×CO_2 (c) G1 (d) difference 4×CO_2-piControl and (e) difference G1-piControl. The red plus sign in a-e indicates latitudes with maximum SSTs. Stipples indicate grid points where difference is statistically significant at 90 % cl using non-parametric Wilcoxon rank sum test. The box in the eastern Pacific identifies the Niño3 region.

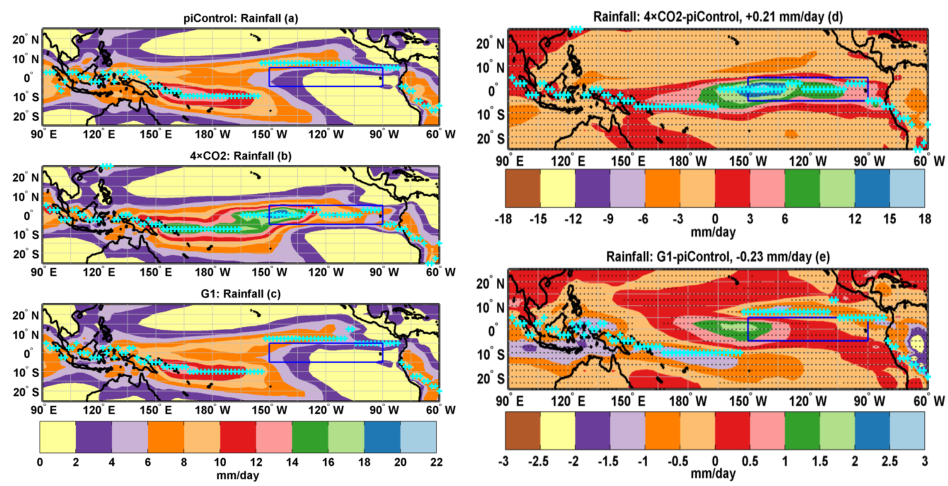

Figure 2. Tropical Pacific rainfall mean DJF climatology (a) piControl (b) 4×CO_2 (c) G1 (d) difference: 4×CO_2-piControl; the cyan plus sign indicate position of ITCZ under 4×CO_2 and (e) difference: G1-piControl; the cyan plus sign indicate position of ITCZ under G1. In a-c the cyan plus indicate position of ITCZ for corresponding experiment. Stipples indicate grid points where difference is statistically significant at 90 % cl using non-parametric Wilcoxon rank sum test.

Atmos. Chem. Phys. Discuss., https://doi.org/10.5194/acp-2018-1312
Manuscript under review for journal Atmos. Chem. Phys.
Discussion started: 7 January 2019

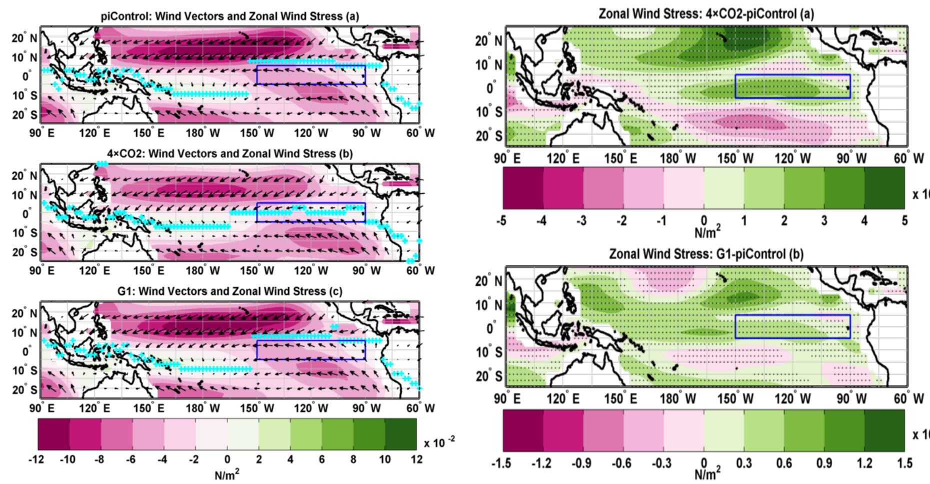

Figure 3. Tropical Pacific zonal wind stress mean DJF climatology (a) piControl (b) 4×CO_2 (c) G1 (d) difference: 4×CO_2-piControl and (e) difference: G1-piControl. Black arrows indicate direction of 10 m wind. The cyan plus sign in a-e indicates latitudes with maximum rainfall. Stipples indicate grid points where difference is statistically significant at 90 % cl using non-parametric Wilcoxon rank sum test.

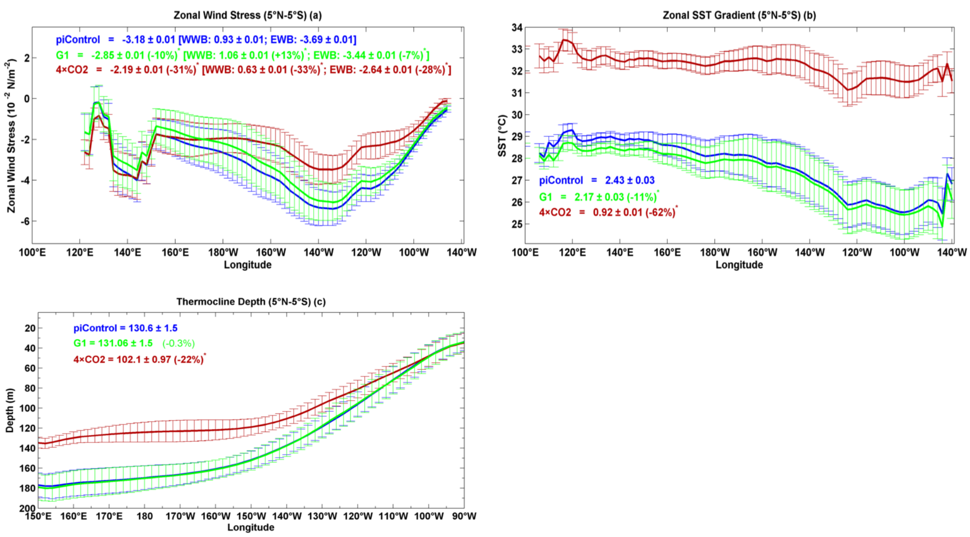

Figure 4. DJF mean climatology of (a) zonal wind stress (b) zonal SST gradient, and (c) thermocline depth. Error bars indicate ±1 s.d. calculated over the simulated period. Numbers with asterisk indicate that the percentage change is statistically significant at 99 % cl.

Atmos. Chem. Phys. Discuss., https://doi.org/10.5194/acp-2018-1312
Manuscript under review for journal Atmos. Chem. Phys.
Discussion started: 7 January 2019

Atmospheric Chemistry and Physics
Discussions

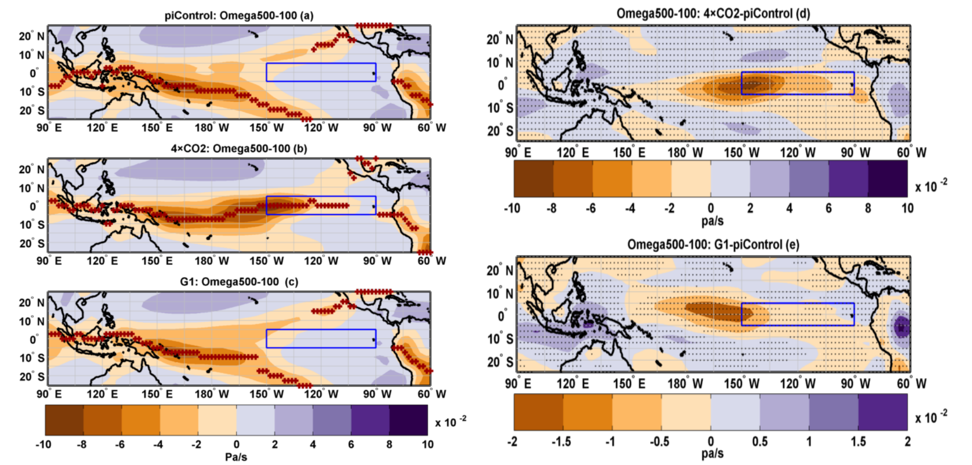

Figure 5. Tropical Pacific mean DJF climatology of vertical velocity averaged between 500- and 100-hPa (Omega500-100) (a) piControl (b) 4×CO_2 (c) G1 (d) difference: 4×CO_2-piControl and (e) difference: G1-piControl. In a-c the brown plus sign indicate latitudes where maximum upwelling occurs. Stipples indicate grid points where difference is statistically significant at 90 % cl using non-parametric Wilcoxon rank sum test.

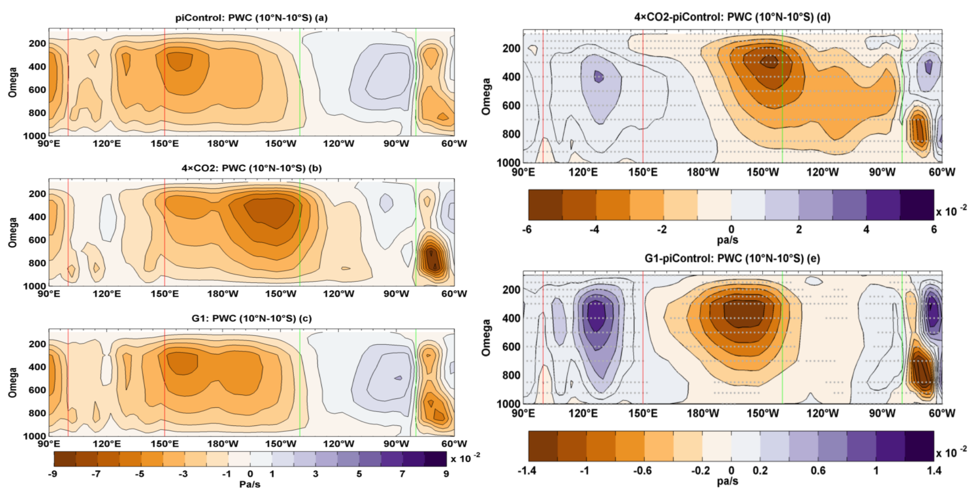

Figure 6. Mean DJF climatology of tropical Pacific Walker Circulation averaged over 90° E-60° W and 10° N-10° S (a) piControl (b) 4×CO_2 (c) G1 (d) difference: 4×CO_2-piControl and (e) difference: G1-piControl. Green (red) vertical lines show longitudinal spread of eastern (western) Pacific. Stipples indicate grid points where difference is statistically significant at 90 % cl using non-parametric Wilcoxon rank sum test.

Atmos. Chem. Phys. Discuss., https://doi.org/10.5194/acp-2018-1312
Manuscript under review for journal Atmos. Chem. Phys.
Discussion started: 7 January 2019

Atmospheric Chemistry and Physics
Open Access
Discussions

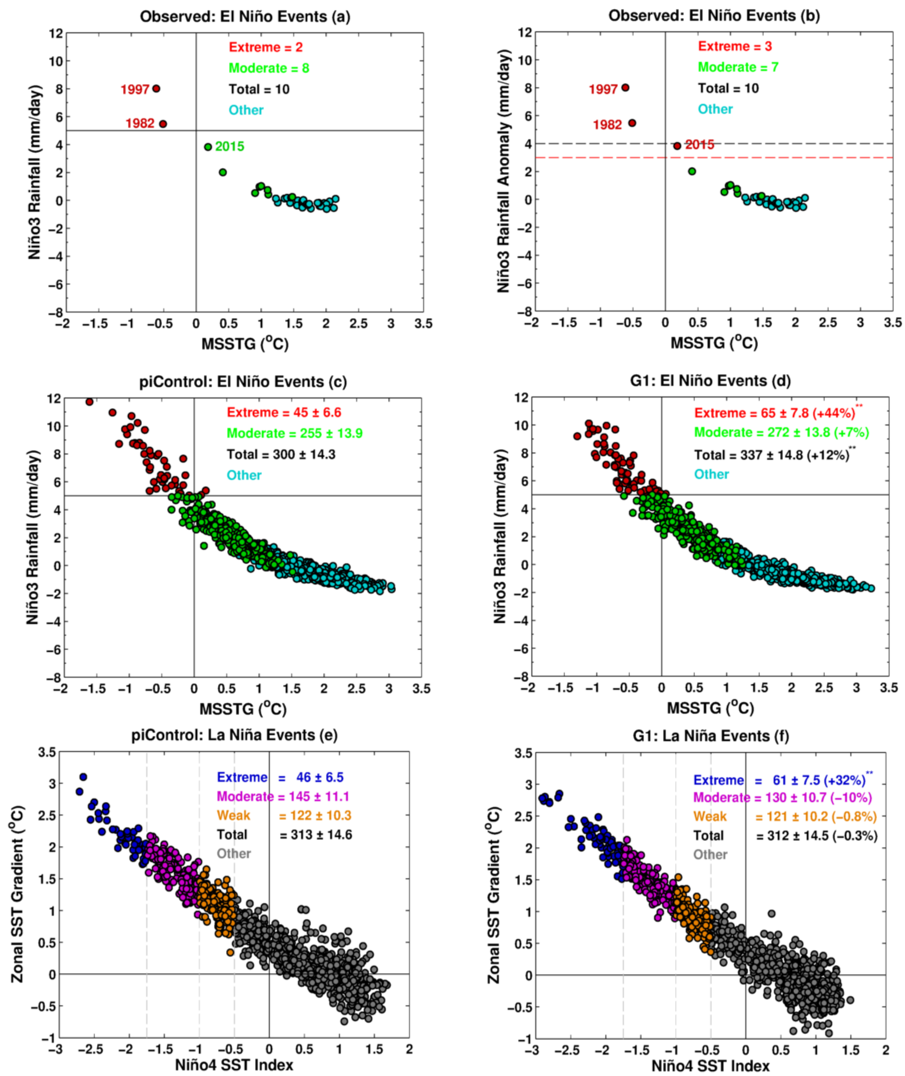

Figure 7. Observed relationship between MSSTG and Niño3 rainfall when extreme El Niño is defined with (a) Niño3 total rainfall > 5 mm day^{-1} (b) Niño3 rainfall anomaly > 3 or 4 mm day^{-1}. Simulated relationship between MSSTG and Niño3 rainfall for (c) piControl (d) G1. Simulated relationship between Niño4 and ZSSTG for (e) piControl and (f) G1. In b the solid black horizontal line indicates threshold value of 5 mm day^{-1}. In a, c and d the dashed red (black) horizontal line indicates threshold anomaly of 3 (4) mm day^{-1}. See text for definition of extreme, moderate, weak, and total El Niño (La Niña) events. The asterisk indicates that the change in frequency is statistically significant at 95 % cl. Numbers with ± symbol indicate s.d. calculated with 10,000 bootstrap realizations.

Atmos. Chem. Phys. Discuss., https://doi.org/10.5194/acp-2018-1312
Manuscript under review for journal Atmos. Chem. Phys.
Discussion started: 7 January 2019

Atmospheric Chemistry and Physics
Discussions
Open Access
EGU

Figure 8.

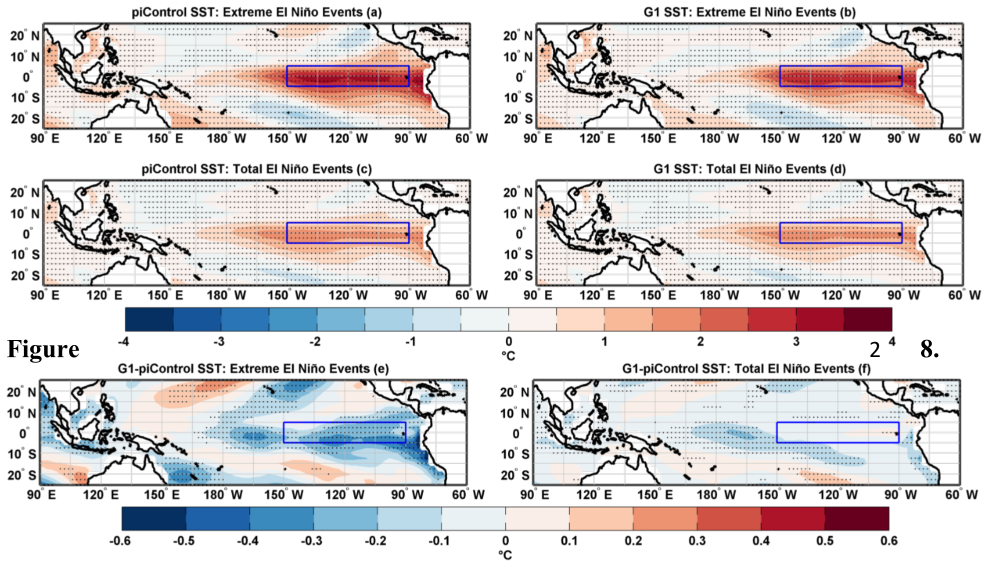

Figure 8. Composites of SST anomalies for extreme El Niño events in (a) piControl (b) G1. Composites of SST anomalies for total number of El Niño events in (c) piControl (d) G1. Composite differences (G1-piControl) of SST anomalies for (e) extreme El Niño events and (f) total number of El Niño events. Stipples indicate grid points with statistical significance at 90 % cl using non-parametric Wilcoxon rank sum test. The box in the eastern Pacific identifies the Niño3 region.

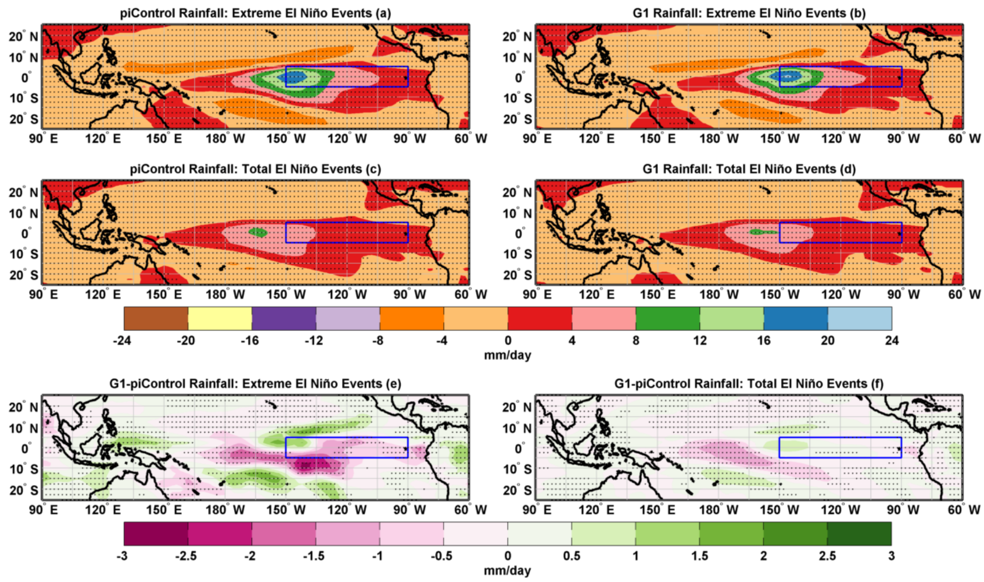

Figure 9. Composites of rainfall anomalies for extreme El Niño events in (a) piControl (b) G1. Composites of rainfall anomalies for total number of El Niño events in (c) piControl (d) G1. Composite differences (G1-piControl) of rainfall anomalies for (e) extreme El Niño events and (f) total number of El Niño events. Stipples indicate grid points with statistical significance at 90 % cl using non-parametric Wilcoxon rank sum test. The box in the eastern Pacific identifies the Niño3 region.

Atmos. Chem. Phys. Discuss., https://doi.org/10.5194/acp-2018-1312
Manuscript under review for journal Atmos. Chem. Phys.
Discussion started: 7 January 2019

Atmospheric Chemistry and Physics Discussions

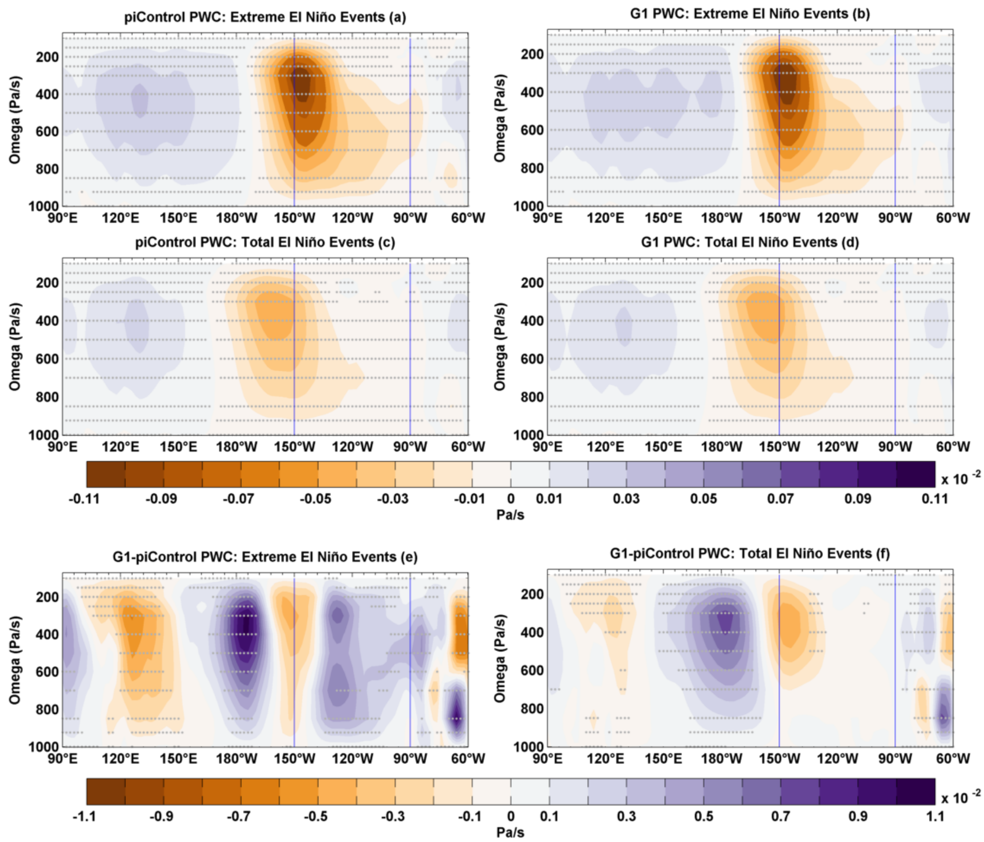

Figure 10. Composites of PWC anomalies for extreme El Niño events in (a) piControl (b) G1. Composites of PWC anomalies for total number of El Niño events in (c) piControl (d) G1. Composite differences (G1-piControl) of PWC for (e) extreme El Niño events and (f) total number of El Niño events. Stipples indicate grid points with statistical significance at 90 % cl using non-parametric Wilcoxon rank sum test. The box indicates the Niño4 region.

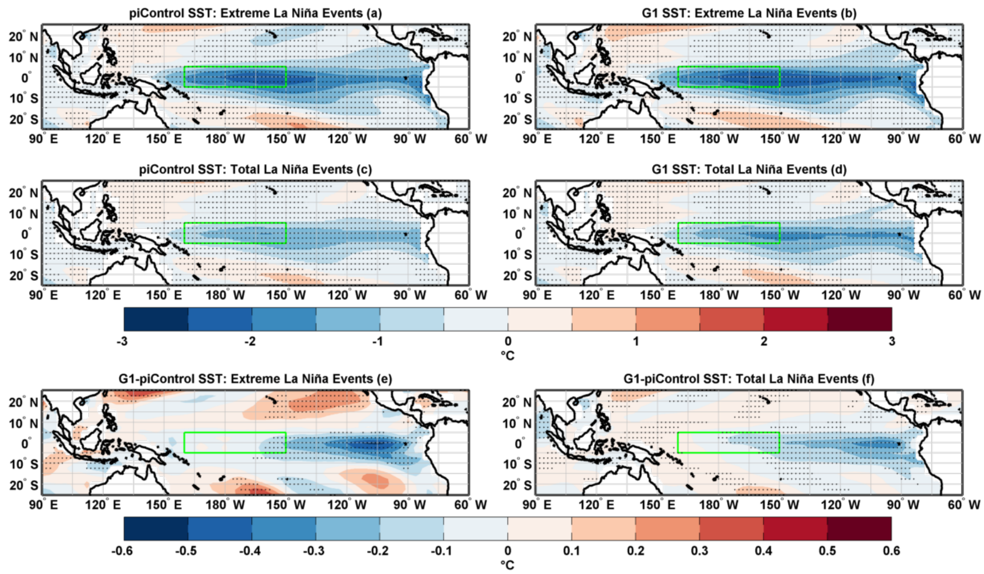

Figure 11. Composites of SST anomalies for extreme La Niña events in (a) piControl (b) G1. Composites of SST for total number of La Niña events in (c) piControl (d) G1. Composite differences (G1-piControl) of SST for (e) extreme La Niña events and (f) total number of La Niña events. Stipples indicate grid points with statistical significance at 90 % cl using non-parametric Wilcoxon rank sum test. The box indicates the Niño4 region.

Atmos. Chem. Phys. Discuss., https://doi.org/10.5194/acp-2018-1312
Manuscript under review for journal Atmos. Chem. Phys.
Discussion started: 7 January 2019

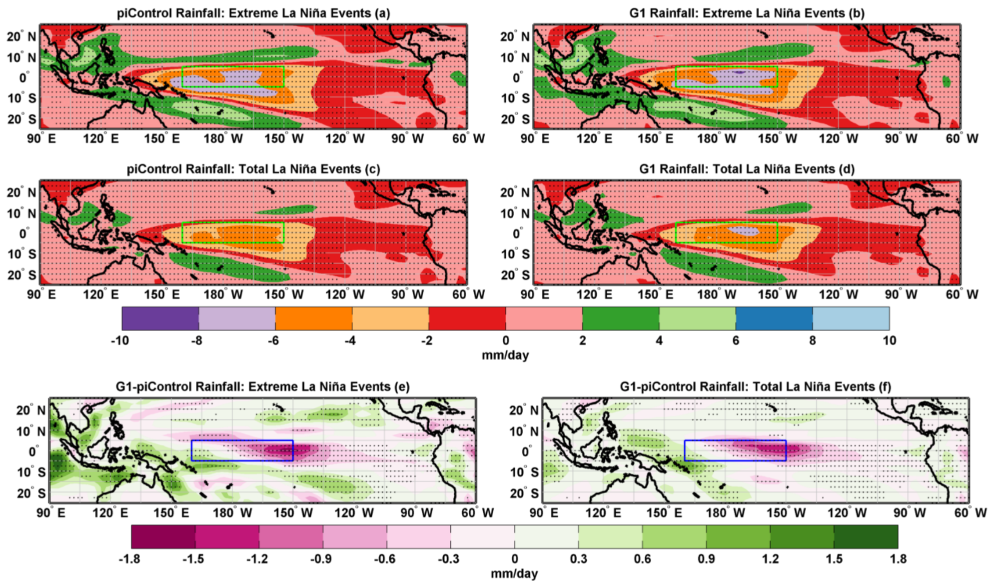

Figure 12. Composites of rainfall anomalies for extreme La Niña events in (a) piControl (b) G1. Composites of rainfall anomalies for total number of La Niña events in (c) piControl (d) G1. Composite differences (G1-piControl) of rainfall for (e) extreme La Niña events and (f) total number of La Niña events. Stipples indicate grid points with statistical significance at 90 % cl using non-parametric Wilcoxon rank sum test. The box indicates the Niño4 region.

Atmos. Chem. Phys. Discuss., https://doi.org/10.5194/acp-2018-1312
Manuscript under review for journal Atmos. Chem. Phys.
Discussion started: 7 January 2019

Atmospheric Chemistry and Physics
Discussions

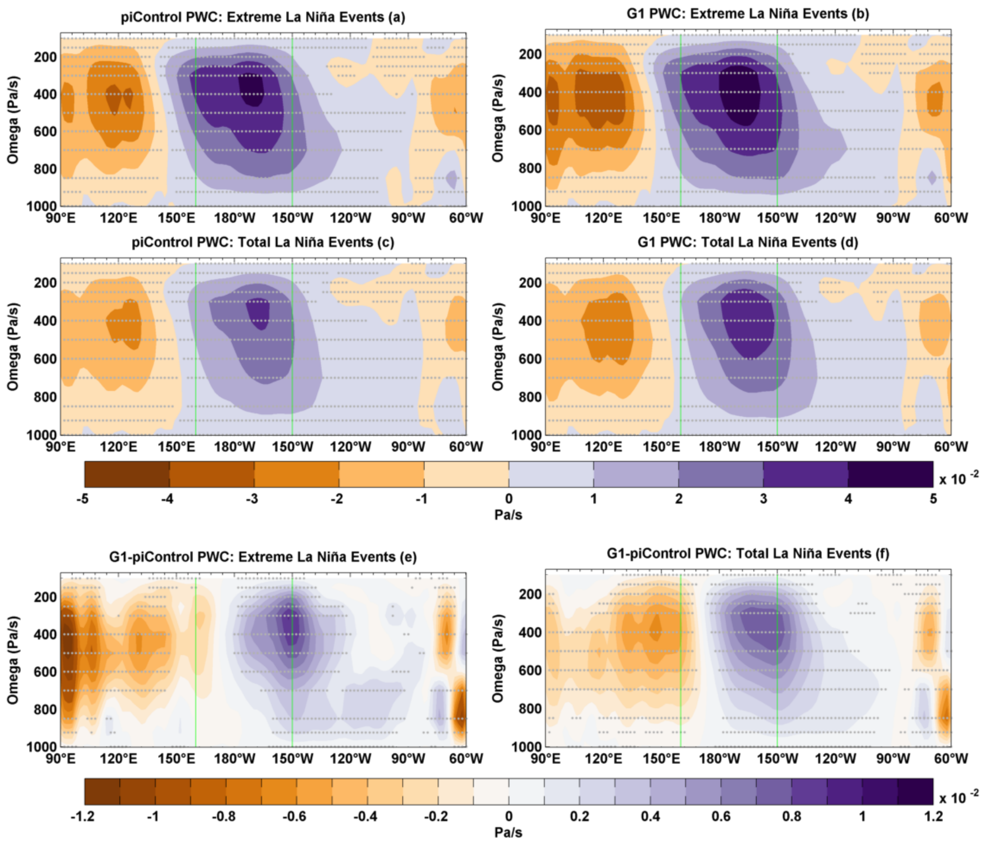

Figure 13. Composites of PWC anomalies for extreme La Niña events in (a) piControl (b) G1. Composites of PWC for total number of La Niña events in (c) piControl (d) G1. Composite differences (G1-piControl) of PWC anomalies for (e) extreme La Niña events and (f) total number of La Niña events. Stipples indicate grid points with statistical significance at 90 % cl using non-parametric Wilcoxon rank sum test.

Tables and Table Captions

Table 1. ENSO amplitude

Experiment	Amplitude (°C)	Difference w.r.t. piControl (°C)	Std. Dev. 10,000 Realizations (°C)	~ Change w.r.t. piControl (%)
piControl	1.04 (0.78) [1.04]		0.0213 (0.0132) [0.0176]	
4×CO_2	0.55 (0.28) [0.49]	-0.49 (-0.50) [-0.55]		-47* (-64*) [-55*]
G1	1.13 (0.79) [1.09]	0.09 (0.01) [0.05]		+8* (+1) [+5**]

Key: Niño3 (Niño4) [Niño3.4]; *99 % cl; **95 % cl

Table 2. Maximum amplitude of warm events

Experiment	Amplitude (°C)	Difference w.r.t. piControl (°C)	Std. Dev. 10,000 Realizations (°C)	~ Change w.r.t. piControl (%)
piControl	2.97 (1.32) [2.34]		0.0687 (0.0159) [0.0367]	
4×CO_2	1.29 (0.92) [1.08]	-1.68 (-0.40) [-1.26]		-57* (-30*) [-54*]
G1	2.85 (1.17) [2.18]	-0.12 (-0.15) [-0.16]		-4 (-11*) [-7*]

Key: Niño3 (Niño4) [Niño3.4]; *99 % cl; **95 % cl

Table 3. Maximum amplitude of cold events

Experiment	Amplitude (°C)	Difference w.r.t. piControl (°C)	Std. Dev. 10,000 Realizations (°C)	~ Change w.r.t. piControl (%)
piControl	-2.31 (-2.13) [-2.42]		0.1439 (0.0459) [0.1452]	
4×CO_2	-1.86 (-1.37) [-1.91]	0.45 (0.76) [0.51]		-19* (-36*) [-21*]
G1	-2.26 (-2.55) [-2.62]	0.05 (-0.42) [-0.20]		-2 (+20*) [+8]

Key: Niño3 (Niño4) [Niño3.4]; *99 % cl; **95 % cl

Table 4. Niño3 SST skewness

Experiment	Skewness	Difference w.r.t. piControl	Std. Dev. 10,000 Realizations	~ Change w.r.t. piControl (%)
piControl	0.52*		0.0542	
4×CO_2	-0.47*	-0.99		-190*
G1	0.18*	-0.34		-65*

Key: *99 % cl; **95 % cl